Crustal structure across the Grand Banks–Newfoundland Basin Continental Margin – I. Results from a seismic refraction profile

K. W. Helen Lau,[1] Keith E. Louden,[1] Thomas Funck,[2,*] Brian E. Tucholke,[3] W. Steven Holbrook,[4] John R. Hopper[2,†] and Hans Christian Larsen[2,‡]

[1]*Department of Oceanography, Dalhousie University, Halifax, Nova Scotia,* B3H 4J1, *Canada. E-mail: kwhlau@dal.ca*

[2]*Danish Lithosphere Center, Øster Voldgade* 10, DK-1350 *Copenhagen K, Denmark*

[3]*Department of Geology and Geophysics, Woods Hole Oceanographic Institution, Woods Hole, Massachusetts* 02543, *USA*

[4]*Department of Geology and Geophysics, University of Wyoming, Laramie, Wyoming* 82071, *USA*

[*] Now at: Dept. of Geophysics, Geological Survey of Denmark and Greenland (GEUS), ØsterVoldgade 10, DK-1350 Copenhagen K, Denmark.

[†]Now at: Dept. of Geology and Geophysics, TexasA&MUniversity, College Station, TX, 77843, USA.

[‡]Now at: IODP-MI Sapporo Office, Rm. 05-101, CRIS, Hokkaido University, N21, W10, Sapporo, 001-0021, Japan.

Accepted 2006 March 3. Received 2006 February 28; in original form 2005 May 18

Abbreviated title for heading: Structure across Newfoundland Basin Margin (I)

Corresponding author: Helen Lau (kwhlau@dal.ca)

Summary

A P-wave velocity model along a 565-km-long profile across the Grand Banks/Newfoundland basin rifted margin is presented. Continental crust ~36-km-thick beneath the Grand Banks is divided into upper (5.8-6.25 km/s), middle (6.3-6.53 km/s) and lower crust (6.77-6.9 km/s), consistent with velocity structure of Avalon zone Appalachian crust. Syn-rift sediment sequences 6-7-km thick occur in

two primary layers within the Jeanne d'Arc and the Carson basins (~3 km/s in upper layer; ~5 km/s in lower layer). Abrupt crustal thinning (Moho dip ~ 35º) beneath the Carson basin and more gradual thinning seaward forms a 170-km-wide zone of rifted continental crust. Within this zone, lower and middle continental crust thin preferentially seaward until they are completely removed, while very thin (<3 km) upper crust continues ~60 km farther seaward. Adjacent to the continental crust, high velocity gradients (0.5-1.5 s^{-1}) define an 80-km-wide zone of transitional basement that can be interpreted as exhumed, serpentinized mantle or anomalously thin oceanic crust, based on its velocity model alone. We prefer the exhumed-mantle interpretation after considering the non-reflective character of the basement and the low amplitude of associated magnetic anomalies, which are atypical of oceanic crust. Beneath both the transitional basement and thin (<6 km) continental crust, a 200-km-wide zone with reduced mantle velocities (7.6-7.9 km/s) is observed, which is interpreted as partially (<10%) serpentinized mantle. Seaward of the transitional basement, 2- to 6-km-thick crust with layer 2 (4.5-6.3 km/s) and layer 3 (6.3-7.2 km/s) velocities is interpreted as oceanic crust. Comparison of our crustal model with profile IAM-9 across the Iberia Abyssal Plain on the conjugate Iberia margin suggests asymmetrical continental breakup in which a wider zone of extended continental crust has been left on the Newfoundland side.

Keywords

Continental margins; crustal structures; refraction seismology; rifted margins

1. Introduction

Non-volcanic continental margins have been studied to understand crustal responses under large amounts of extension because their extensional fabrics are not overprinted by excessive syn-rift melt. Comparisons of structures from conjugate margins are particularly useful due to the importance of understanding asymmetry in margin development. The earliest such study by Keen *et al.* (1989) compared deep seismic reflection structures across the Flemish Cap-Goban Spur conjugates in the North Atlantic. They observed that while crustal thinning was symmetric across the rift, as in a pure shear model (McKenzie 1978), asymmetrical continental breakup left a wider zone of the rifted continental crust on the Goban Spur side. A subsequent study across the Labrador-southwest Greenland conjugates by Chian *et al.* (1995) provided a better constrained comparison from coincident reflection and refraction data. They observed that crustal thinning was symmetric until the final stage of rifting, when an asymmetrical detachment fault cut through the crust, decoupling the southwestern Greenland upper plate from the Labrador lower plate. This also resulted in zones of transitional basement, interpreted as exhumed mantle, which are wider on the Labrador side. The lack of comparable studies from other conjugate margins, however, has prevented us from knowing if a general pattern exists in the asymmetry of non-volcanic margins.

The Newfoundland-Iberia margin conjugates provide an excellent opportunity for new studies of conjugate non-volcanic margins as the Iberia margin has already been well sampled by seismic surveys and drilling. However, until recently, a detailed comparison with the structures on the Newfoundland margin was

impossible because of a lack of coincident reflection and refraction data at relevant conjugate locations. Therefore, a large-scale seismic survey (SCREECH, Study of Continental Rifting and Extension on the Eastern Canadian sHelf) was conducted on the eastern Grand Banks-Newfoundland basin margin in 2000 (Fig. 1). Three major transects of coincident multi-channel seismic (MCS) and wide-angle reflection/refraction data were collected (Lines 1, 2 and 3). Line 1 is the profile across the Flemish Cap margin, which is conjugate to the Galicia Bank margin. Structure on these margins shows that the zone of rifted continental crust is much wider on the Galicia Bank margin, while crustal thinning is more rapid on the Flemish Cap margin (Funck *et al.* 2003; Hopper *et al.* 2004). Asymmetry also exists in the transition zone farther seaward; exhumed mantle is observed on the Galicia Bank margin (Whitmarsh *et al.* 1996; Boillot *et al.* 1987), while oceanic crust appears to be present immediately seaward of rifted continental crust on the Flemish Cap margin.

Farther to the south, profile IAM-9 across the Iberia Abyssal Plain (Pickup *et al.* 1996; Dean *et al.* 2000) shows a much narrower zone of rifted continental crust and a much wider zone of exhumed mantle compared to Galicia Bank. On the conjugate Newfoundland basin margin, serpentinized mantle has been suggested beneath rifted continental and oceanic crust (Reid 1994) and exhumed mantle has been drilled at ODP Site 1277 (Leg 210; Shipboard Scientific Party 2004). To further define the suggested asymmetry across the conjugates and along strike variation in structure, a detailed comparison between structures across the conjugates is required.

In this study, we present results from SCREECH Line 3, the southernmost profile (Fig. 1), which is roughly conjugate (~140 km offset; Srivastava *et al.* 2000) to profile IAM-9 on the Iberia margin. Line 3 crosses the east central Grand Banks, the southern Jeanne d'Arc, Carson, and north Salar basins, and the Newfoundland basin north of the Newfoundland Seamounts. A velocity model derived from the wide-angle data is presented in this paper, and a companion paper (Lau *et al.*, 2006) discusses the coincident MCS data. Our goal is to define the margin structure, to detail the nature of the rifted continental crust, transitional basement, and oceanic crust, and to investigate the degree of serpentinization in the mantle. These features are compared with those of IAM-9 (Dean *et al.* 2000). They are also compared with results from the Flemish Cap (Hopper *et al.* 2004; Funck *et al.* 2003) and Galicia Bank conjugates (González *et al.* 1999; Whitmarsh *et al.* 1996). We find a wide layer of low-velocity mantle that we interpret as partially serpentinized mantle. This layer is observed on the landward side beneath very thin continental crust and it extends seaward beneath transitional basement that we suggest is exhumed, highly serpentinized mantle, similar to observations on the Iberia margin. We show that the Newfoundland margin has a much wider zone of rifted continental crust than the Iberia margin, indicating that continental breakup was asymmetrical. This asymmetry is opposite in orientation to that of the Flemish Cap-Galicia Bank conjugates. Thus, our results show that variations in asymmetry related to the development of a wide-rift not only exist between margin segments, as previously known, but also within a margin segment.

2. Geological setting

Beneath the Grand Banks (Fig. 1), pre-rift Appalachian continental crust is separated by the Collector magnetic anomaly into the Avalon Terrane to the north and the Meguma Terrane to the south (Haworth & Lefort 1979). The velocity structure of these terranes is well defined by previous data. This crust was subsequently rifted in two or three phases (e.g., Tankard & Welsink, 1987; Tucholke & Whitmarsh, in press): (1) late Triassic rifting formed major rift basins in the continental crust of Grand Banks (e.g., the Jeanne d'Arc basin; Fig. 1); (2) late Jurassic (Oxfordian-Kimmeridgian) rifting affected many of these basins; and (3) latest Jurassic to early Cretaceous rifting between Newfoundland and Iberia led to breakup and formation of oceanic crust. The syn-rift sediment sequences in Jeanne d'Arc basin have been well studied by drilling and MCS data (e.g. Keen *et al.* 1987; Driscoll *et al.* 1995). The lower sequence is defined by bedded salt deposited during the Triassic phase of rifting, while the upper sequence was deposited during the later phases.

Prior to the present study, crustal structure farther seaward beneath the Newfoundland basin was poorly constrained, and conflicting interpretations had been proposed for the origin of basement. Existing data allowed for the possibility that an ocean-continent transition exists in the Newfoundland basin where the basement could be: (1) oceanic or ultra-slow spreading oceanic crust (Keen & de Voogd 1988; Reid 1994; Srivastava *et al.* 2000); (2) thinned continental crust (Tucholke *et al.* 1989; Enachescu 1992); or (3) exhumed mantle as observed on the conjugate Iberia margin (e.g. Boillot *et al.* 1987; Dean *et al.* 2000).

The first hypothesis of anomalously thin oceanic crust is suggested by refraction Line 7 (Reid 1994) in Fig. 1. This line is the only wide-angle seismic profile that reaches the deeper basin and is also coincident with an MCS reflection profile (Lithoprobe 85-2; Keen & de Voogd 1988). The velocity model for Line 7 (Fig. 2) shows that the continental crust has a maximum thickness of ~28 km and consists of three crustal layers (with velocities of 5.7, 6.0 and 6.7 km/s). The continental crust thins abruptly seaward of the shelf break until it reaches zero thickness at an interpreted continent-ocean boundary (COB) near 120 km model distance. A change in velocities seaward of the COB indicates that a layer of 4.5 km/s, interpreted as oceanic crust, is observed below the basement surface. This layer is anomalously thin (1-4 km thick) and has a rather low velocity for oceanic crust. Beneath it, layers of 7.2 and 7.7 km/s, interpreted as serpentinized mantle, were observed above unaltered mantle (8.0 km/s). Srivastava *et al.* (2000) also suggested that oceanic crust exists seaward of ~90 km, based on interpretation of low-amplitude magnetic anomalies as being formed by slow seafloor spreading (half rate = 6.7 mm/yr) as early as chron M20 (~139 Ma; timescale of Kent & Gradstein 1985).

A second possibility, interpreted from MCS observations, is that a wide zone of thin continental crust exists beneath the Newfoundland basin (Tucholke *et al.* 1989; Enachescu 1992). However, interpretations of the MCS data within this area were ambiguous due to weak basement reflectivity beneath a high amplitude and reverberative sedimentary reflection referred to as the "U"-reflection (Tucholke *et al.* 1989; for details see Lau *et al.*, this issue).

The third possibility, exhumed mantle, is derived from observations on the conjugate Iberia margin. Extensive geophysical surveys (e.g. Dean *et al.* 2000; Chian *et al.* 1999; Reston *et al.* 1996; Pickup *et al.* 1996, Boillot *et al.* 1987) have suggested the presence of exhumed serpentinized mantle seaward of extended continental crust under the Iberia Abyssal Plain, and serpentinized peridotite has been drilled there during ODP Legs 149 and 173 (Sawyer *et al.* 1994; Whitmarsh *et al.* 1998). After the onset of the present study, ODP Site 1277 (Leg 210) along SCREECH Line 2 (Fig. 1) in the Newfoundland basin also drilled serpentinized mantle (Shipboard Scientific Party 2004).

3. Methods

a) Data acquisition and processing

The SCREECH experiment included collection of wide-angle seismic data along three transects (Lines 1, 2 and 3; Fig. 1), using ocean bottom hydrophones and seismometers (hereafter, OBS) deployed from R/V Oceanus as receivers, and an 8540 cu. in. (140 L), 20-airgun tuned array deployed from R/V Maurice Ewing as source. For Line 3, sensors included hydrophones in all OBS, and three-component, 4.5-Hz geophones in 11 instruments (Table 1); sampling rates were 5 ms, 5.734 ms or 7.168 ms depending on instruments (see Table 1 for details). A total of 24 OBS were deployed initially for the main shooting of Line 3 (Fig. 1, Table 1). Instrument spacing ranged from 50 km over the continental shelf to 10-40 km over deeper water. The shot spacing was 50 m over the shelf region up to OBS 5 (Fig. 1) and 200 m for the remainder of the profile. Subsequently, two OBS (25 and 26) were re-

deployed on the continental slope to record additional shots at 50-m intervals from near offsets. OBS 24 was lost and two OBS (20 and 21) failed to record. Hence, we had data available from a total of 23 stations.

OBS data were synchronized to GPS time. OBS positions on the seafloor were determined by least-squares fits to the observed arrival times of the direct wave. STD (Salinity-Temperature-Depth) measurements collected at two locations on Line 3 were used to determine the water velocity structure and HYDROSWEEP® centre-beam data were used to measure water depth. The RMS errors in range as determined between relocated OBS positions and shot positions compared with those determined from direct wave arrivals are given in Table 1. The estimated horizontal distances over which the OBS drifted from their deployment locations to their sea bottom positions are also given in Table 1.

In this study, only the vertical geophone and the hydrophone data were analyzed for velocity modelling. OBS data were debiased (i.e. mean amplitude equals zero) and bandpass filtered. Spiking deconvolution was applied to records that resulted in a sharpening of the signals and improvement in the delineation of second arrivals. Record sections (Figs 3-9) are displayed with a reduction velocity of 6.5 km/s.

b) Data modelling

A 565-km-long velocity model was set up along a great-circle arc defined by the shot points at either end of Line 3. The maximum deviations of the corrected OBS locations and shot positions from this great circle arc were 1.175 km and 0.830 km, respectively. We used the RAYINVR and TRAMP algorithms (Zelt & Smith

1992) to determine the P-wave velocity model. Initially, a forward model was developed from the top to the bottom layer. Coincident MCS data along line 3 (Lau *et al.*, this issue) were used to adjust the detailed geometry of the model sedimentary layers and the basement. The resulting model was then refined by inversion for the velocities and depths of the continental crustal layers and the low-velocity mantle layer, which are well sampled by wide-angle data.

c) Wide-angle data

Figures 3-9 show record sections from seven instruments located at critical regions of the profile. Record sections for the other OBS are shown in Appendix A. Data are characterized by high signal-to-noise ratios for most stations; only three instruments (OBS 5, 8 and 18) have low signal-to-noise ratios. Arrivals are observed up to a range of 260 km. Theoretical travel-time curves computed by ray tracing through the final model (Fig. 10a) are included for comparison. Phases are named according to later interpretations of the corresponding layers as defined in Table 2.

The main observations in the record sections are described below, starting with OBS 4 at the landward end of the line and moving to OBS 19 at the seaward end. The northwestern side of the OBS 4 record (Fig. 3) provides constraints on sedimentary velocities within the Jeanne d'Arc basin and on crustal thickness and velocities of the upper and middle crust at the continental end of the model. For the lower sedimentary layer in Jeanne d'Arc basin, a high velocity (~5.4 km/s) refraction phase (P_{SY2}) is observed. For the crust, the refraction phases from the upper crust have very low amplitude in nearer offsets (P_{c1}), possibly due to divergence of rays in the Jeanne d'Arc basin. The phase velocity of the refraction through the crust is ~6.5

km/s toward larger offsets (P_{c2}). A weak intra-crustal reflection ($P_{c2}P$) between the middle and lower crust is intermittently observed from -50 to -120 km offset. Refractions from the lower crust (P_{c3}) can be observed on OBS 1 and 2 (Figs A1 and A2; Appendix A) to constrain its velocity. The full crustal thickness is constrained by the high-amplitude, wide-angle Moho reflection (P_mP).

The southeastern side of the OBS 4 record shows evidence for a major change in crustal thickness and basement structure seaward near the shelf break. The P_{c1} phase has an average phase velocity of ~5.4 km/s; this is very different from the actual crustal velocity (5.8-6.25 km/s) because of the presence of another rifted basin and seaward deepening of the basement. The abrupt changes in the geometry of the wide-angle Moho reflection (P_mP) also indicate a large change in crustal thickness. Furthermore, the mantle phase (P_{n2}), with phase velocity ~8.0 km/s, is observed at a minimum offset of 100 km, whereas no P_{n2} phase is observed on the northwest side of the record. This suggests thinner crust seaward.

OBS 9 (Fig. 4) is located where the continental crust thins to < 4 km and the middle and the lower crust eventually pinch out just to the southeast above a layer of low-velocity mantle. A thick sedimentary sequence is observed and phases from a total of five sedimentary layers ($P_{S[1-5]}$, $P_{S[1-5]}P$) are identified (Fig. A8; Appendix A). The reflection phases can be correlated with major reflections on the coincident MCS section (Lau *et al.*, this issue). Multiple crustal layers on the northwestern side are evidenced by the wide-angle reflection from the top of the lower crust ($P_{c2}P$) at ~15-20 km offsets, distinctive from the P_mP phase that arrives later. In contrast, intra-crustal reflections are absent on the southeastern side, suggesting a single

crustal layer. To the southeast, a refracted phase from the mantle (P_{n1}, phase velocity ~7.7 km/s) had to be modelled with a velocity lower than that used to fit the P_{n2} phase to the northwest. This requires a separate mantle layer with a lower velocity (7.6-8.0 km/s) in the southeastern part of the model. This P_{n1} phase becomes a first arrival immediately after the deepest sedimentary phase P_{S5}, and the P_{c1} phase only appears as a second arrival, implying very thin crust to the southeast.

OBS 10 (Fig. 5) provides constraints on the velocity structure of the seaward-most part of the upper continental crust. The P_{c1} phase is modelled with a velocity of ~5.8 km/s, similar to that at the neighbouring station OBS 9. This indicates continuity of velocity layering with the upper crust farther landward. P_mP phases are observed on both sides, though more apparently on the northwest side. They constrain the Moho depths and suggest a velocity discontinuity across a thin gradient zone, because no Moho reflection is observed in the MCS data (Lau *et al.*, this issue).

On OBS 12 (Fig. 6), the thickness of the upper continental crust approaches zero. The P_{c1} phase on the northwest side is restricted to offsets <18 km. The mantle phase (P_{n1}) appears as a first arrival at offsets of ~13 km, indicating the presence of very thin crust. Within the sediment, the "U"-reflection, which is a high-amplitude reflection on the coincident MCS data (Lau *et al.*, this issue), is observed as a prominent reflection phase in the wide-angle data.

OBS 15 (Fig. 7) indicates a new crustal regime, as the velocity structure is very different from that landward (c.f. OBS 9). Two new basement phases (P_{T1} and P_{T2}) are introduced; these are continuous and are modelled by a strong gradient in

the upper layer and a phase velocity of ~7.4 km/s in the bottom layer. No sub-basement reflections could be identified, suggesting the absence of any major first-order velocity discontinuities there.

OBS 17 (Fig. 8) indicates a transition to another crustal regime at the seaward end of the profile. The low-velocity mantle layer (P_{n1}) is well constrained by travel times and by the amplitude which drops dramatically from the phase P_{n1} to the phase P_{n2} (at ~ -77 km offset). This is caused by the decrease in velocity gradient from low-velocity mantle to normal mantle. A strong Moho reflection (P_mP) is observed in both wide-angle and MCS data (Lau *et al.*, this issue). On the seaward, southeastern side, a new crustal phase (P_{L2}) with a phase velocity of ~6.5 km/s is observed, indicating refraction through the upper part of the crust seaward. According to the model result, the P_{L2} phase extends to the southeast and adjoins a separate phase (P_{L3}) representing refraction through the lower part of the crust, in which the velocities are better defined by OBS 19 farther seaward. Note that a refracted phase with a phase velocity of 4.6 km/s, indicated by a question mark in Fig. 8, is not observed in adjacent stations and it therefore was not modelled.

OBS 19 (Fig. 9) shows a better example of the two new crustal phases (P_{L2}, P_{L3}) where they become first arrivals to the southeast as the crust thickens. The gradient is higher in the upper layer than in the lower layer. Their low apparent velocities of ~5.8 km/s, especially to the southeast, are due to basement topography. The mantle phase does not become a first arrival until offsets of ~24 km, indicating a much thicker crust than landward beneath OBS 17.

4. Results

a) Velocity Model

Fig. 10(a) shows the final P-wave velocity model obtained from forward and inverse modelling of the observed traveltimes. The model is divided into sedimentary, crustal and mantle layers. Sediments (above the red line) are thin (<2 km) beneath the shelf except in the two rift basins (Jeanne d'Arc and Carson basins), but they become ~6-km thick seaward of the shelf edge. Velocities increase with depth from 1.6 to 4.5 km/s, except for the bottom layer within the rift basins and over the shelf (distance 0-150 km) where velocities increase to 5.4 km/s. In Carson basin, a high velocity bottom layer (~5.2 km/s) is observed in data of OBS 6, 25 and 26 (Fig. 10b). The similar dimension of the upper and lower layers in Jeanne d'Arc and Carson basins suggests two major sequences of thick (6-7 km) syn-rift sediments (Fig. 10a), as interpreted by Lau *et al.* (this issue). From comparison with the well studied Jeanne d'Arc basin (e.g. Keen *et al.* 1987; Driscoll *et al.* 1995; Sinclair 1995), the high-velocity (highly compacted) bottom sequence in Carson basin probably was deposited during Late Triassic rifting while the crust was still thick. The low-velocity (less compacted) upper sequence probably was deposited during the Late Jurassic to Early Cretaceous rifting.

The 34-37 km thick continental crust observed beneath the Grand Banks (distance 0-220 km) can be divided into upper (5.8-6.25 km/s), middle (6.3-6.53 km/s) and lower (6.77-6.9 km/s) layers. The velocity gradient is greater (~0.04 s^{-1}) in the upper crust and smaller in the lower crust (~0.01 s^{-1}). Crustal thinning that formed the Jeanne d'Arc basin is restricted to the upper crust. However, the crust

thins seaward from 34 to 10 km (initial thickness/crustal thickness, ß ~ 2.3) from distance 220 to 250 km (Moho dip ~ 35º); most of this appears to be taken up by thinning in the lower crust (ß ~ 2.8). A large upper-crustal basement high forms a fault block at distance 250-270 km, and the crust thins more gradually seaward. The middle and the lower continental crust disappear at distance 330 km, but the model layer of thin (<3 km) upper crust extends farther seaward to distance 380 km. The velocity of the upper crust decreases only slightly to ~5.5-6.0 km/s seaward of distance ~300 km.

The basement at distance 385-465 km has velocities and gradients very different from those farther landward. The velocity gradients are high (0.9-1.5 s^{-1} for the upper layer; 0.5 s^{-1} for the lower layer) and there is a smooth velocity transition between the layers. P-wave velocities are 4.4-6.4 km/s and 6.4-7.8 km/s in the upper and lower layer, respectively. These basement layers are slightly elevated with respect to the continental crust landward, are characterized by highs at the two ends (distance ~395 and 465 km) with very flat topography in between (Lau *et al.*, this issue), and represent a transition zone between the crustal layers to either side.

From distance 465 km to the seaward end of the profile, the model shows velocity structures compatible with oceanic crust. The ~2-km-thick crust at 465-470 km could be resolved as only one layer with velocities of 4.5-6.3 km/s and is interpreted as oceanic layer 2. At distances >470 km, layer 3 (6.3-7.2 km/s) thickens until the total crustal thickness is ~4.7 km, with the thickest crust at distance 490-510 km beneath the J-anomaly (a high-amplitude magnetic anomaly between M0 and

M1; Rabinowitz *et al.* 1979). Lower-crustal velocities increase to 6.9-7.5 km/s toward the seaward end of the line according to results from OBS 22.

Seaward of distance 285 km, a low-velocity mantle layer (up to ~5-km thick, with velocities of 7.6-8.0 km/s) is first observed when the overlying continental crust thins to <6 km. Velocities in this layer increase downward into normal mantle velocities (7.9-8.0 km/s) and adjoin at the base with normal mantle of lower velocity gradient. This layer becomes very thin and approaches normal mantle velocities seaward of distance 490 km beneath the oceanic layer 3.

b) Model Uncertainty and Resolution

Standard statistical error analyses were done to assess model accuracy (e.g. Zelt & White 1995). The root-mean-square misfits (t_{rms}) between observed and calculated travel times for each phase and station were calculated. These misfits were also normalized to values of χ^2 using the uncertainty for each pick (varying between 20 and 300 ms depending on the signal-to-noise ratio). Results are summarized in Table 3. The total misfit is 0.153 s and total normalized χ^2 is 1.837. The higher value for the upper continental crustal phase (P_{c1}) is due to misfits in data from OBS 4, 25 and 7, which are located just above the steeply sloping flanks of two basement blocks and are difficult to model precisely. The higher values of normalized χ^2 for the transitional layer phases are not reflected in their misfits (71 and 77 ms for P_{T1} and P_{T2}, respectively), but are related to their small pick uncertainties.

Fig. 10(b) shows the ray path coverage of the model to qualitatively represent the resolution of the model. Regions covered by a large amount of horizontal (or

turning) ray paths are considered highly resolved. For a quantitative approach, a diagonal value of the resolution matrix (Zelt & Smith 1992) was obtained for each velocity and depth node (Figs 10d and e). Nodes with values >0.5 are typically considered well resolved (Lutter & Nowack 1990). Regions of good velocity resolution in our model include the three upper sediment layers in the Newfoundland basin, the thick continental crust, part of the thinned upper crust, most of the thinned middle crust, the low-velocity mantle layer, and the mantle wedge immediately seaward of the thick crust. Regions with poor velocity resolution (<0.3) are the deeper sediments including rifted basins, the thinned lower crust, the transitional basement, oceanic layer 3, and the seaward part of the normal mantle. Note that the velocity resolutions for areas between nodes are interpolated by gridding and should be interpreted with care.

Depth nodes are well resolved (>0.5) for sediments and basement, intra-crustal and Moho boundaries of the continental crust (0-200 km), the base of middle crust and the Moho beneath the large basement high (250-290 km), the base of the crust at 305-375 km and 470-550 km, and the bottom of layer 2 at 525-555 km. Poorly resolved depth nodes (<0.3) are found along steep boundaries (e.g. the thinning of lower, middle and upper continental crust), the bottom of the upper crust at 250-285 km and at boundaries without a velocity discontinuity (e.g. bottom of transitional crust and the bottom of layer 2 at 475-525 km).

Because the transitional basement (distance 385-465 km) has very low resolution, we present an additional velocity model (Model B; Fig. 11b) that agrees equally well with the OBS data as the model described above (Model A; Fig. 11a).

The primary difference is that Model B has a thinner lower basement layer with a lower velocity gradient and a velocity discontinuity at the base. The middle panels of Fig. 11 show the synthetic sections derived for both models at OBS 14 with similar filtering applied and noise level. While Model A, which predicts no wide-angle Moho (P_mP), fits the amplitude pattern better on the southeastern side, Model B is able to match the amplitude pattern better on the northwestern side with a possible P_mP phase observed at offsets -10 to -15 km. Similar uncertainty occurs at other stations over the transitional basement (c.f. OBS 15 and 16). Therefore, the low resolution of this part of the model permits either the presence or absence of a velocity discontinuity at the base of the lower transitional basement layer.

c) Gravity Modelling

Fig. 12 shows the satellite-derived free-air gravity anomaly for the survey area (Sandwell & Smith 1997). The gravitational edge effect (i.e. a maximum followed by a minimum across the continental shelf edge and slope) is well demonstrated along the margin of the Grand Banks except for the area around Line 3. Amplitude changes there are more subdued and complex in both dip and strike directions. Part of this complexity may be caused by the large basement block at 250-275 km in our velocity model.

Although these features suggest that a 2-D density model may be an oversimplification, we developed such a model consistent with our velocity model to investigate first-order correlations between the data sets (Fig. 13). We used the methodology of Talwani *et al.* (1959) and Won & Bevis (1987). The geometry of the density model was taken from the layer boundaries in the velocity model and the

density in each layer was obtained from conversion of the P-wave velocity using well-established density-velocity relationships (Fig. 14; Hughes *et al.* 1998; Christensen & Mooney 1995; Ludwig *et al.* 1970). The calculated values fit the general pattern of the observed gravity (Fig. 13, upper panel), considering that the observed gravity varies by as much as 80 mGal within 40 km to either side of the model plane.

The calculated pressures at the bottom of the model are equal at the two ends (Fig. 13; bottom panel), indicating that our model is regionally isostatically balanced. However, an offset in pressure from a lower general value landward to a higher value seaward occurs at ~250 km model distance. Such an offset may be compensated by modelling with a slightly higher mantle density (e.g. 3.3 Mg/m^3) beneath the thicker continental crust. However, this would increase the gravity anomalies at the landward end of the model to values that are significantly higher than observed. A reasonable fit may require a thicker sediment layer at the landward end than is defined in the model, which is poorly constrained by the MCS data.

Some modifications to this model were necessary to reduce the misfit between the predicted anomaly and the observed anomalies. These include thickening the landward part of the crust outside the ray coverage (distance 0-20 km) and lowering the density of the low-velocity mantle layer from that suggested by the density-velocity relationship (3.25 Mg/m^3; Fig. 14) to 3.15 Mg/m^3. The latter modification reduced the calculated gravity by a maximum of ~17 mGal and the RMS error (misfit) by ~4 mGal (or ~18%). The largest misfit occurs for distances 100-240 km. A better fit (dashed line), with RMS error reduced by ~5 mGal (or

~27%), requires that the upper crustal thickness does not increase seaward so that higher densities are present at shallower levels. This modification, however, conflicts with our velocity model, in which the upper crustal thickness is constrained by data from OBS 2, 3 and 4 (Fig. 3), with high resolution at ~155 km distance. Therefore, this modification is presented only as an alternative model for comparison.

5. Discussion

a) Continental crust

We have compiled velocity-depth profiles from Appalachian continental crust on the Grand Banks (Fig. 15) for comparison to Line 3 (Fig. 10). Haworth & Lefort (1979) have used the magnetic Collector Anomaly to separate the Avalon zone to the north from the Meguma Terrane to the south (Fig. 12). The velocity structure of our thickest crust on Line 3 (Fig. 10) is consistent with previous results for the Avalon zone (Fig. 15a). For example, the total crustal thickness (35 km) and average velocity (~6.5 km/s) of Line 3 are very similar to those of model AC1 (Marillier *et al.* 1994), a well constrained model near Newfoundland. It is also very similar in velocity to model AC3 on Flemish Cap (average velocity ~6.4 km/s; Funck *et al.* 2003) although the crust underneath Flemish Cap is 5 km thinner than at the other locations. On the other hand, the Meguma models are different from Line 3 (Fig. 15b). They have crustal velocities generally 0.1-0.4 km/s lower than Line 3 and the crust is also thinner by ~5-8 km. These differences highlight the regional variations of the crust beneath the Grand Banks.

Although the velocity structure of Line 3 is similar to that of the Avalon Terrane, there may be significant local variations in this terrane. For example, velocity model AC2 seems to conflict with the model of Line 3 in that it exhibits a high-velocity (~7.2 km/s) lower crust that was interpreted as magmatic underplating (Reid & Keen 1990). This is, however, the only Grand Banks velocity model where underplating has been proposed. Therefore, we revisited the data for model AC2 and found that for the main profile, the refracted phase through the underplated layer is obscured by the reverberations from earlier phases. Good evidence only comes from arrivals from a short line shot out-of-plane to two OBS. Because Line 3 shows no evidence for this layer beneath the Grand Banks, such underplating is probably only a local feature not sampled by Line 3.

b) Ocean-continent transition

The best resolved and largest-scale feature of the OCT is the low-velocity mantle layer (Fig. 10). We attribute the low-velocity layer to a low degree of serpentinization (<10% based on velocities; Horen *et al.* 1996; Christensen 1966; Miller & Christensen 1997), caused by seawater penetrating through the overlying basement. This is possible when the overlying crust becomes entirely brittle (Pérez-Gussinyé & Reston 2001). Here, this occurs when the crust is less than 6 km thick (distances >285 km), slightly less than that proposed by the simple 1-D thermal models of Pérez-Gussinyé & Reston (2001). This thickness controls the landward limit of the serpentinized mantle layer and this limit is coincident with a landward dipping reflector "L" (Lau *et al.*, this issue). The low-velocity mantle layer continues

seaward to ~490 km, where we interpret oceanic crust that seals the mantle from seawater.

Above the layer of low-velocity mantle and seaward of the pinch-out of the lower continental crust (distance 330 km), there is a 60-km-wide zone with an extremely thin basement layer that we interpret as upper continental crust. This interpretation is based on the following: (1) the velocity structure, with good constraints (Fig. 10), shows high crustal velocity (5.6-6.0 km/s) and low gradient (0.1-0.3 s^{-1}) that connect smoothly with those of the well constrained continental crust landward; and (2) its character (see below) in seismic reflection (MCS) and wide-angle data is more like that of continental crust than it is of other basement types such as exhumed serpentinized mantle or oceanic crust. To illustrate the second point, Fig. 16 shows a comparison of velocity structure and reflectivity between our interpreted continental section and a section of basement interpreted as exhumed, serpentinized mantle beneath the Iberia Abyssal Plain (IAM-9; Dean *et al.* 2000; Pickup *et al.* 1996). On Line 3, the crust is characterized by large fault blocks ~20-km-wide and a basement relief of ~2 km, whereas the structures on IAM-9 are narrower and somewhat more subdued. Furthermore, the crust on Line 3 is characterized by a single velocity layer whereas the exhumed mantle on the Iberia margin consists of two velocity layers with increased reflectivity in the lower layer (Pickup *et al.* 1996). Therefore the two sections are unlikely to be of the same basement type. The section on Line 3 is also very different from ultra-slow spreading oceanic crust such as that observed on Line 1 (Funck *et al.* 2003; Hopper *et al.* 2004), which has very high reflectivity and velocities consistent with oceanic layers

2 and 3. Finally, in terms of basement relief, the Line 3 section is comparable to that of tilted fault blocks of thin upper continental crust on the deep western margin of Galicia Bank (Reston *et al.* 1996).

Above the low-velocity mantle layer and seaward of the interpreted thin continental crust, transitional basement is observed at distance 385-465 km. Its velocity structure is poorly resolved, and two alternate models (A and B; Fig. 11) provide a reasonable fit to the data. Neither model resembles continental crust because of the presence of high velocity gradients. We suggest that the transitional basement may represent a prolonged adjustment stage between continental extension and seafloor spreading when atypical basement, such as exhumed serpentinized mantle or anomalously thin oceanic crust, was emplaced (Fig. 17). If interpreted as exhumed mantle, the basement layer (4.4-7.8 km/s) of Model A indicates a degree of serpentinization from 100% at the top to ~4% near the base (Horen *et al.* 1996; Christensen 1966; Miller & Christensen 1997). In Model B, the "Moho" would represent a serpentinization front that separates more highly serpentinized mantle from much less serpentinized mantle underneath. Alternatively, Model B can also be interpreted as thin oceanic crust with oceanic layers 2 and 3 in the upper and lower layers, respectively, based on its similarity in velocities to those of typical Atlantic oceanic crust (Fig. 18; White *et al.* 1992). In contrast, Model A exhibits velocities too high at the base of its lower layer (7.5-8.0 km/s) for typical oceanic crust. An exception would be if additional ultra mafic rock, such as serpentinized peridotite, is added to the lower crust to achieve these high velocities. We prefer the exhumed, serpentinized mantle interpretation based on two observations: (1) the magnetic

anomalies in this zone are very weak (Fig. 17; Srivastava *et al.* 2000); and (2) the basement has subdued relief and is unreflective (Fig. 17; Lau *et al.*, 2006). These observations are unusual for normal oceanic crust, which generally is more reflective and has a rough, faulted surface, especially if it is formed at very low spreading rates. The low reflectivity of the layer is more like that of the exhumed, serpentinized mantle on profile IAM-9 (Pickup *et al.* 1996).

c) Oceanic crust

Fig. 18 shows a comparison between velocity-depth structure at three locations (distances 500, 520, 540 km) within the zone of interpreted oceanic crust and that of typical Atlantic oceanic crust (White *et al.* 1992). The velocities are compatible with typical oceanic crust except at the seaward-most location (540 km) where the lower-crustal velocity is <0.3 km/s higher than normal. However, the anomalously high velocities at this location are poorly resolved (resolution <0.2) and they may be caused by the complex structures near the top of basement shown in the MCS data (Lau *et al.*, this issue). At the landward part of the zone of interpreted oceanic crust (distances 500 and 520 km), the velocities of the lower crustal layer are compatible with typical oceanic layer 3 (White *et al.* 1992), except for near the top where the velocities are too low (>6.3 km/s). However, the velocities in this part are poorly constrained (resolution ~ 0.3; Fig. 10d). Furthermore, the low velocities near the top may imply that layer 2 may be thicker than is defined in the model as the depths of the layer 2/layer 3 boundary are poorly constrained (resolution ~ 0).

The crustal thickness changes seaward from ~6.0 to 4.3 km and it is thinner than typical oceanic crust (Fig. 18). However, interpreted oceanic crust ~5-km-thick

is also observed beneath the Iberia Abyssal Plain (Dean *et al.* 2000). Thus, the thinner part of the oceanic crust at these margins may have been slightly extended during periods of low magma supply. A heterogeneous and anomalously thin oceanic crust, possibly formed by slow or ultra-slow spreading, is also observed on the seaward ends of SCREECH Lines 1 and 2 (e.g., Hopper *et al.* 2004; Van Avendonk *et al.*, in review).

d) Iberia conjugate and reconstruction

Profile IAM-9 (Dean *et al.* 2000) across the southern Iberia Abyssal Plain is the refraction profile most nearly conjugate to Line 3 (it is offset ~140 km to the north; Srivastava *et al.* 2000). Figs 19(a) & (b) show a reconstruction between the Newfoundland basin - Iberia Abyssal Plain (hereafter, NB-IAP) conjugates at the time of (a) interpreted separation of continental crust, and (b) the J-anomaly. As on the Iberia margin landward of the J-anomaly (Fig. 18b), Line 3 exhibits a layer of serpentinized mantle beneath thin, low-velocity basement that we interpret as serpentinite. Thus, mantle exhumation and serpentinization appears to have occurred on both margins before oceanic crust was formed. Despite these similarities, the NB-IAP conjugates at the time of separation of continental crust (Fig. 19a) appear to have been highly asymmetrical, with breakup focused at the Iberia edge of the rift and a section of very thin upper continental crust left on the Newfoundland side. Such significant asymmetry may be related to the large width (~270 km) of the rift. In existing numerical models and observations of wide rifts (>100 km), breakup occurs along one edge of the rift, thus forming a narrow/wide conjugate margin pair (Dunbar & Sawyer 1989; Hopper & Buck 1996).

Additional asymmetrical features shown on Fig. 19(a) may or may not be significant. For example, the gradual thinning of the Iberia continental crust is different from the more abrupt thinning of the Newfoundland crust beneath Carson basin, especially within the lower crust (Fig. 19a). However, there is no reason to expect large rift basins to be symmetrically distributed on both sides of the rift. Furthermore, margin-parallel structural changes probably occur over the ~140 km along-strike offset (Srivastava *et al.* 2000) between Line 3 and profile IAM-9. Finally, the Iberia margin is depicted without a middle crustal layer. However, the Iberia crustal structure landward of distance 35 km is constrained only by gravity data (Dean *et al.* 2000), so the lack of a middle crust is likely just a modelling preference.

Fig. 19(a) suggests that before breakup, the continental crust was thinned more-or-less symmetrically about an axis at ~ 40 km from the breakup location on the Newfoundland basin margin. Thinning occurred preferentially within the lower crust, which was symmetrically and completely removed from the central part of the rift. Unlike the Galicia Bank margin where a strong sub-horizontal reflection is observed under the thinned continental crust (Fig. 19c), suggesting a detachment surface (Reston *et al.* 1996), such a reflector is absent on both Line 3 (Fig. 16; Lau *et al.*, this issue) and IAM-9 (Pickup *et al.* 1996). Therefore, our observations do not support the hypothesis that an asymmetrical detachment fault exists across the NB-IAP conjugates to form a pair of upper- and lower-plate margins, as suggested by a simple shear model (Wernicke 1985).

There are, however, several explanations for the preferential thinning of the lower crust. The first possibility is that the lower crust was thinned by ductile deformation to allow depth-dependent thinning. A similar process has been proposed for the Northern Carnarvon basin, Australia (Driscoll & Karner 1998) and South China Sea margin (Clift & Lin 2001). However, the ductile-brittle boundary needs to be as shallow as the upper/lower crustal boundary, which is probably invalid for highly thinned crust <6-km-thick (Pérez-Gussinyé & Reston 2001). Another possibility is that velocities of the lower and middle crust were reduced to upper crustal velocities by faulting as it cooled to become brittle or by expansion due to lower pressures at shallower depths. In this case, only the total crustal thinning is constrained by the velocity model. However, the upper part of the crust is likely to be true upper crust because the reflectivity suggests traces of pre-rift sediments above the seaward-most part of the interpreted continental crust (Lau *et al.*, this issue). A third possibility may be that part of the lower crust was somehow lost during rifting to out-of-plane locations but this hypothesis has not been confirmed. Alternatively, part of the lower crust from Line 3 might be left on the unobserved side of a truly conjugate pair of profiles (Line 3 and IAM-9 are offset by ~140 km; Srivastava *et al.* 2000). Further investigations are needed for a better understanding of the causes of preferential thinning in the lower crust.

For the transitional basement, Srivastava *et al.* (2000) suggested emplacement by slow seafloor spreading, based on interpretation of low-amplitude magnetic anomalies. Their results would suggest oceanic crust dating to as old as anomaly M17 (distance ~120 km; Fig. 19b) on the Newfoundland basin margin and

also on the conjugate Iberia Abyssal Plain margin (seaward of distance ~120 km). This interpretation, however, conflicts with the seismic characteristics on the Iberia Abyssal Plain margin that indicate the presence of serpentinized mantle. The transitional basement of the NB-IAP margin conjugates also has a reflective character that is significantly different from that of anomalously slow spreading oceanic crust as observed on Line 1 seaward of Flemish Cap (Funck *et al.* 2003; Hopper *et al.* 2004). Furthermore, by also comparing with the MCS data of nearby profiles, Lau *et al.* (this issue) concluded that oceanic crust can only be interpreted seaward of distance ~40 km on the Newfoundland basin margin (Fig. 19b).

Fig. 19(c) shows the Flemish Cap-Galicia Bank (hereafter, FC-GB) conjugates at the position of SCREECH Line 1, reconstructed to chron M0 (Funck *et al.* 2003). Like the NB-IAP conjugates, a layer of partially serpentinized mantle is observed on both sides of the FC-GB conjugates, but a peridotite ridge is developed on the Galicia Bank margin. The serpentinized layer has a thickness similar to that of the NB-IAP conjugates.

Several major differences are observed between the NB-IAP and FC-GB conjugates:

(1) Continental crust on the FC-GB conjugates rifted apart shortly before anomaly M0, significantly later than the crustal separation in the NB-IAP conjugates (Figs 19b and c). This is consistent with the idea that the Newfoundland-Iberia rift opened from south to north (e.g., Srivastava *et al.* 2000).

(2) The total width of the zone of exhumed, serpentinized mantle on the FC-GB conjugates appears to be only ~10 km and it is restricted to the Galicia side, in contrast to 80 and 170 km widths of these zones on the NB-IAP conjugates.

(3) Margin asymmetry on the FC-GB conjugates (wide zone of thinned continental crust on the east, and narrow on the west) is reversed on the NB-IAP conjugates (compare Figs 19b and c).

(4) A strong sub-horizontal "S"-reflection, interpreted as a detachment surface, is present beneath Galicia Bank in the FC-GB section (Reston *et al.* 1996), but it is absent on the NB-IAP conjugates.

(5) Anomalously thin oceanic crust is present off the Flemish Cap in the FC-GB section (Funck *et al.* 2003; Hopper *et al.* 2004), but it appears not to be present on the NB-IAP conjugates. Note that the interpreted oceanic crust on the two sides of the FC-GB section appears to have different thicknesses at chron M0 (Fig. 19c). However, Funck *et al.* (2003) argued that the lower layer (layer 3) off Galicia is possibly the serpentinized mantle layer. If so, the oceanic crust on both conjugates was anomalously thin (~3.3 km) before M0, and it probably resulted from limited melt emplacement during ultra-slow spreading (Funck *et al.* 2003; Hopper *et al.* 2004).

All of the features outlined above indicate that the parts of the margin represented in the NB-IAP and FC-GB transects rifted in very different styles. Thus

it appears that a transfer zone is present between the two conjugate pairs and that it accommodated the along-strike transition in rift style.

6. Conclusions

We developed a 2-D velocity model across the Grand Banks-Newfoundland basin using new coincident wide-angle and MCS data. Interpretation of the velocity model in conjunction with the MCS data allows the following conclusions:

(i) Continental crust beneath the Grand Banks is 34-37 km thick and consists of an upper (5.8-6.25 km/s), middle (6.3-6.53 km/s) and lower crust (6.77-6.9 km/s). This velocity structure is consistent with that of the Avalon zone of Appalachian crust but it is different from that of crust in the Meguma Terrane.

(ii) During rifting of the upper crust, the Jeanne d'Arc and the Carson basins were filled with two major sequences of syn-rift sediment with a total thickness of 6-7 km. The lower sequence (~5.2 km/s) was deposited during the Late Triassic rifting and the upper sequence (3.2 km/s) was deposited during Late Jurassic to Early Cretaceous rifting.

(iii) Abrupt crustal thinning (Moho dip ~ 35º) is observed beneath the Carson basin, and it is followed by more gradual thinning seaward of a large basement high at the eastern edge of the basin. The rifting formed a zone of extended continental crust ~170-km-wide. The seaward 60 km of this zone is interpreted as thin (<3 km) upper continental crust. Its velocities and reflectivity are unlike those of the exhumed, serpentinized mantle observed on the conjugate Iberia margin (Pickup *et al.* 1996; Dean *et al.* 2000) and are also different from those of

anomalously thin oceanic crust observed seaward of Flemish Cap (Line 1; Funck *et al.* 2003; Hopper *et al.* 2004).

(iv) Beneath continental crust less than 6-km thick and transitional basement farther seaward, we observe a 5 to 6-km-thick layer with velocities of 7.6-8.0 km/s. This layer is interpreted as partially (<10%) serpentinized mantle. It extends over a width of ~200 km across the Newfoundland basin and ends where interpreted oceanic crust appears near magnetic anomaly M4.

(v) An ~80-km-wide zone of transitional basement is observed between thinned continental crust and basement interpreted as normal oceanic crust. We are unable to discriminate between two models for the transitional basement, both of which are characterized by high velocity gradients (0.5-1.5 s^{-1}). Both models can be interpreted as either exhumed, serpentinized mantle or anomalously thin oceanic crust. Considering the non-reflective character of the basement and the low amplitude of associated magnetic anomalies, we prefer the interpretation that the transition zone consists of exhumed, serpentinized mantle.

(vi) Crust with velocities characteristic of oceanic Layer 2 (4.5-6.3 km/s) and Layer 3 (6.3-7.2 km/s) is observed seaward of the transitional basement out to the end of the profile.

Reconstruction of the Newfoundland-Iberia margin near-conjugate profiles (~140 km offset; Srivastava *et al.* 2000) at the time of separation of continental crust suggests the following:

(i) Asymmetry in the distribution of thin continental crust on the Newfoundland basin-Iberia Abyssal Plain conjugates is consistent with a wide-rift model in

which final breakup was located along the edge of the Iberia margin. The zone of thinned continental crust is ~170-km wide on the Newfoundland margin and ~80-km wide on the Iberia margin.

(ii) No asymmetrical detachment faults are observed on either conjugate. Instead, we observe preferential thinning of the lower crust on the Newfoundland margin and apparently on the Iberia Abyssal Plain margin. The lower-crustal thinning could be caused by ductile deformation in the lower crust, or it could be only apparent, i.e. a reduction in velocities of lower crust by faulting and expansion. It is also possible that part of the lower crust was lost to out-of-plane locations or left on the unobserved side of a pair of true conjugates.

(iii) As rifting progressed northward to the Flemish Cap-Galicia Bank conjugates, the width of exhumed serpentinized mantle became narrower, the breakup of continental crust shifted toward the Flemish Cap margin, major detachment at the base of the thinned continental crust controlled rifting on the Galicia Bank margin, and ultra-slow spreading oceanic crust was formed seaward. This indicates that a major along-strike transition in margin architecture was present between the Newfoundland basin-Iberia Abyssal Plain conjugates and the Flemish Cap-Galicia Bank conjugates.

Acknowledgments

We thank the scientific staff, officers and crew on board the R/V Oceanus and R/V Maurice Ewing for their diligent work at sea. In particular, we thank Robert Iuliucci and Walter Judge from Dalhousie University, and David DuBois, Robert

Handy, Kenneth Peal and James Ryder from Woods Hole Oceanographic Institution, who were in charge of OBS operations on board R/V Oceanus. We also thank the reviewer, R.S. White, and the editor, T.A. Minshull, for their comments on this manuscript. This research was supported by National Science Foundation (NSF) grants OCE-9819053 and OCE-0326714, by the National Sciences and Engineering Research Council of Canada (NSERC), and by the Danish National Research Foundation. B. Tucholke also acknowledges support from the Henry Bryant Bigelow Chair in Oceanography from Woods Hole Oceanographic Institution. Contribution No. 11,378 of Woods Hole Oceanographic Institution.

References

Boillot, G., Winterer, E.L., Meyer, A.W. & Shipboard Scientific Party, 1987. *Proceedings of the Ocean Drilling Program, Initial Reports*, Vol.103, ed. Littleton, R.M., Ocean Drilling Program, College Station, TX.

Chian, D., Louden, K.E. & Reid, I., 1995. Crustal structure of the Labrador Sea conjugate margin and implications for the formation of nonvolcanic continental margins, *J. Geophys. Res.,* **100**, 24239-24253.

Chian, D., Louden, K.E., Minshull, T.A. & Whitmarsh, R.B., 1999. Deep structure of the ocean-continental transition in the southern Iberia Abyssal Plain from seismic refraction profiles: Ocean Drilling Program (Legs 149 and 173) transect, *J. Geophys. Res.,* **104**, 7443-7462.

Christensen, N.I., 1966. Elasticity of Ultrabasic Rocks, *J. Geophys. Res.*, **71**, 5921-5931.

Christensen, N.I. & Mooney, W.D., 1995. Seismic velocity structure and composition of the continental crust; a global view, *J. Geophys. Res.*, **100(6)**, 9761-9788.

Clift, P. & Lin, J., 2001. Preferential mantle lithospheric extension under the South China margin, *Marine and Petroleum Geology*, **18**, 929-945.

Contrucci, I., Klingelhöfer, F., Perrot, J., Bartolome, R., Gutscher, M.-A., Sahabi, M., Malod, J. & Rehault, J.-P., 2004. The crustal structure of the NW-Moroccan continental margin from wide-angle and reflection seismic data, *Geophys. J. Int.*, **159(1)**, 117-128.

Dean, S.M., Minshull, T.A., Whitmarsh, R.B. & Louden, K.E., 2000. Deep structure of the ocean-continent transition in the southern Iberia Abyssal Plain from seismic refraction profiles: The IAM-9 transect at 40^{o}20'N, *J. Geophys. Res.*, **105**, 5859-5885.

Driscoll, N.W. & Karner, G.D., 1998. Lower crustal extension across the Northern Carnarvon basin, Australia: Evidence for an eastward dipping detachment, *J. Geophys. Res.*, **103(B3)**, 4975-4991.

Driscoll, N.W., Hogg, J.R., Christie-Blick, N. & Karner, G.D., 1995. Extensional tectonics in the Jeanne d'Arc Basin, offshore Newfoundland: implications for the timing of break-up between Grand Banks and Iberia, in *The Tectonics, Sedimentation and Palaeoceanography of the North Atlantic Region*, pp.1-28, eds Scrutton, R.A., Stoker, M.S., Shimmield, G.B. & Tudhope, A.W., Geological Society Special Publication No. 99, The Geological Society, London.

Dunbar J.A. & Sawyer D.S., 1989. Patterns of continental extension along the

conjugate margins of the Central and North Atlantic Oceans and Labrador Sea, *Tectonics*, **8**, 1059-1077.

Enachescu, M.E., 1992. Enigmatic basins offshore Newfoundland. *Canadian Journal of Exploration Geophysics*, **28(1)**, 44-61.

Funck, T., Hopper, J.R., Larsen, H.C., Louden, K.E., Tucholke, B.E.& Holbrook, W.S., 2003. Crustal structure of the ocean-continent transition at Flemish Cap: Seismic refraction results, *J. Geophys. Res.*, **108(B11)**, 2531, doi:10.1029/2003JB002434.

González, A., Córdoba, D., & Vales, D., 1999. Seismic crustal structure of Galicia continental margin, NW Iberian Peninsula, *Geophys. Res. Lett.*, **26(8)**, 1061-1064.

Haworth, R.T. & Lefort, J.P., 1979. Geophysical evidence for the extent of the Avalon zone in Atlantic Canada, *Canadian Journal of Earth Sciences*, **16**, 552-567.

Hopper, J.R. & Buck, W.R., 1996. The effect of lower crustal flow on continental extension and passive margin formation, *J. Geophys. Res.*, **101**, 20175-20194.

Hopper, J.R., Funck, T., Tucholke, B.E., Larsen, H.C., Holbrook, W.S., Louden, K.E., Shillington, D. & Lau, H., 2004. Continental breakup and the onset of ultra-slow seafloor spreading off Flemish Cap on the Newfoundland rifted margin, *Geology*, **32**, 93-96, doi:10.1130/G19694.1.

Horen, H., Zamora, M. & Dubuisson, G, 1996. Seismic wave velocities and anisotropy in serpentinized peridotites from Xigaze ophiolite: Abundance of serpentine in slow spreading ridge, *Geophys. Res. Lett.*, **23(1)**, 9-12.

Hughes, S., Barton, P.J. & Harrison, D., 1998. Exploration in the Shetland-Faeroe Basin using densely spaced arrays of ocean-bottom seismometer, *Geophys.*, **63(2)**, 328-334.

Keen, C.E. & de Voogd, B., 1988. The continent-ocean boundary at the rifted margin off eastern Canada: new results from deep seismic reflection studies, *Tectonics*, **7**, 107-124.

Keen, C.E., Boutilier, R., de Voogd, B., Mudford, B. & Enachescu, M.E., 1987. Crustal geometry and extensional models for the Grand Banks, eastern Canada: constraints from deep seismic reflection data, in *Sedimentary Basins and Basin-Forming Mechanisms*, pp. 101-115, ed. Beaumont, C. & Tankard, A.J., Canadian Society of Petroleum Geologists, Alberta.

Keen, C.E., Peddy, C., de Voogd, B. & Mathews, D., 1989. Conjugate margins of Canada and Europe: results from deep reflection profiling, *Geology*, **17**, 173-176.

Kent, D.V. & F.M. Gradstein, 1985. A Cretaceous and Jurassic geochronology, *Geol. Soc. Amer. Bull.*, **96**, 1419-1427.

Lau, K.W.H., Louden, K.E., Deemer, S., Hall, J., Hopper, J.R., Tucholke, B.E., Holbrook, W.S. & Larsen, H.C, this issue. Crustal Structure across the Grand Banks-Newfoundland Basin Continental Margin (Part II) – Results from a Seismic Reflection Profile, *Geophys. J. Int.*, **XXX**, XXX-XXX.

Louden, K.E., Tucholke B.E. & Oakey, G.N., 2004. Regional anomalies of sediment thickness, basement depth and isostatic crustal thickness in the North Atlantic Ocean, *Earth Planet. Sci. Lett.*, **224**, 193-211.

Ludwig, J.W., Nafe, J.E. & Drake, C.L., 1970. Seismic refraction, *The Sea*, **4(1)**, 53-

84.

Lutter, W.J. & Nowack, R.L., 1990. Inversion for crustal structure using reflections from the PASSCAL Ouachita experiment, *J. Geophys. Res.*, **95**, 4633-4646.

Marillier, M. *et al.*, 1994. Lithoprobe East onshore-offshore seismic refraction survey - constraints on interpretation of reflection data in the Newfoundland Appalachians, *Tectonophysics*, **232**, 43-58.

McKenzie, D.P., 1978. Some remarks on the development of sedimentary basins, *Earth Planet. Sci. Lett.*, **40**, 25-32.

Miller, D.J. & Christensen, N.I., 1997. Seismic velocities of lower crustal and upper mantle rocks from the slow-spreading Mid-Atlantic Ridge, south of the Kane Transform zone (MARK), in *Proceedings of the Ocean Drilling Program, Scientific Results*, Vol. 153, pp. 437-454, ed. Stokking, L., Ocean Drilling Program, College Station, TX.

Pérez-Gussinyé, M. & Reston, T.J., 2001. Rheological evolution during extension at nonvolcanic rifted margins: Onset of serpentinization and development of detachments leading to continental breakup, *J. Geophys. Res.*, **106(B3)**, 3961-3975.

Pickup, S.L.B., Whitmarsh, R.B., Fowler, C.M.R. & Reston, T.J., 1996. Insight into the nature of the ocean-continent transition off West Iberia from a deep multichannel seismic reflection profile, *Geology*, **24**, 1079-1082.

Rabinowitz, P.D., Cande, S.C. & Hayes, D.E., 1979. The J-anomaly in the central North Atlantic Ocean, in *Initial Reports of the Deep Sea Drilling Project*, Vol. 43, pp. 879-885, ed. Kaneps, A., Ocean Drilling Program, College Station, TX.

Reid, I., 1988. Crustal structure beneath the southern Grand Banks: seismic-refraction results and their implications, *Can. J. Earth Sci.*, **25**, 760-772.

Reid, I.D., 1994. Crustal structure of a nonvolcanic rifted margin east of Newfoundland, *J. Geophys. Res.*, **99**, 15161-15180.

Reid, I.D. & Keen, C.E., 1990. Deep crustal structure beneath a rifted basin: results from seismic refraction measurements across the Jeanne d'Arc basin, offshore eastern Canada, *Can. J. Earth Sci.*, **27**, 1462-1471.

Reston, T. J., Krawczyk, C. M. & Klaeschen, D., 1996. The S reflector west of Galicia (Spain): evidence from prestack depth migration for detachment faulting during continental breakup, *Journal of Geophysical Research*, **101(B4)**, 8075-8091.

Sandwell, D.T. & Smith, W.H.F., 1997. Marine gravity anomaly from ERS1, Geosat and satellite altimetry, *J. Geophys. Res.*, **103(5)**, 10039-10045.

Sawyer, D.T., Whitmarsh, R.B., Klaus, A. & Shipboard Scientific Party, 1994. *Proceedings of the Ocean Drilling Program, Initial Reports*, Vol. 149, ed. Stewart, S.K., Ocean Drilling Program, College Station, TX.

Shipboard Scientific Party, 2004. Leg 210 summary, in *Proc. Ocean Drill. Program, Init. Repts.*, Vol. 210, pp. 1-78, eds Tucholke, B.E., Sibuet, J.-C., Klaus, A., Ocean Drilling Program, College Station, TX.

Sinclair, I.K., 1995. Transpressional inversion due to episodic rotation of extensional stresses in Jeanne d'Arc Basin, offshore Newfoundland, in *Basin Inversion*, pp. 249-271, eds Buchanan, J.G. & Buchanan, P.G., Geological Society, London.

Srivastava, S.P., Sibuet, J.-C., Cande, S., Roest, W.R. & Reid, I.R., 2000. Magnetic

evidence for slow seafloor spreading during the formation of the Newfoundland and Iberian margins, *Earth Planet. Sci. Lett.*, **182**, 61-76.

Talwani, M., Worzel, J.L. & Landisman, M., 1959. Rapid gravity computations for two-dimensional bodies with application to the Mendocino submarin fracture zone, *J. Geophys. Res.*, **64**, 49-59.

Tankard, A.J. & Welsink, H.J., 1987. Extensional tectonics and stratigraphy of Hibernia oil field, Grand Banks, Newfoundland, *Am. Ass. Petrol. Geol. Bull.*, **71**, 1210-1232.

Todd, B.J., Reid, I. & Keen, C.E., 1988. Crustal structure across the Southwest Newfoundland Transform Margin, *Can. J. Earth Sci.*, **25**, 744-759.

Tucholke, B.E. & Whitmarsh, R.W., in press. The Newfoundland-Iberia conjugate rifted margins, in *Principles of Phanerozoic Regional Geology*, eds Bally, A.W. & Roberts, D.G., Elsevier, Amsterdam.

Tucholke, B.E., Austin Jr, J.A. & Uchupi, E, 1989. Crustal structure and rift-drift evolution of the Newfoundland Basin, in *Extensional tectonics and stratigraphy of the North Atlantic Margins*), pp. 247-263, eds Tankard, A.J. & Balkwill, H.R., American Association of Petrology and Geology, Tulsa.

Van Avendonk, H. J. A., Holbrook, W. S., Nunes, G. T., Shillington, D. J., Tucholke, B. E., Louden, K. E., Larsen, H. C. & Hopper, J. R., in review. Seismic velocity structure of the rifted margin of the eastern Grand Banks of Newfoundland, Canada, *J. Geophys. Res.*

Wernicke, B., 1985. Uniform-sense normal simple shear of the continental lithosphere, *Can. J. Earth Sci.*, **22**, 108-125.

White, R.S., McKenzie, D. & O'Nions, K., 1992. Oceanic crustal thickness from seismic measurements and rare earth element inversions, *Journal of Geophysical Research*, **97**, 19683-19715.

Whitmarsh, R.B. & Miles, P.R., 1995. Models of the development of the west Iberia rifted continental margin at 40°30'N deduced from surface and deep-tow magnetic anomalies, *J. Geophys. Res.*, **100**, 3789-3860.

Whitmarsh, R.B., Beslier, M.-O., Wallace, P.J. & Shipboard Scientific Party, 1998. *Proceedings of the Ocean Drilling Program, Initial Reports*, Vol. 173, ed. Riegel, R.N., Ocean Drilling Program, College Station, TX.

Whitmarsh, R.B., White, R.S., Horsefield, S.J., Sibuet, J., Recq, M. & Louvel, V., 1996. The ocean-continent boundary off the western continental margin of Iberia: Crustal structure west of Galicia Bank, *Journal of Geophysical Research*, **101(B12)**, 28291-28314.

Won, I.J. & Bevis, M., 1987. Computing the gravitational and magnetic anomalies due to a polygon: Algorithms and Fortran subroutines, *Geophysics*, **52**, 232-238.

Zelt, C.A. & Smith, R.B., 1992. Seismic traveltime inversion for 2-D crustal velocity structure, *Geophys. J. Int.*, **108**, 16-34.

Zelt, C.A. & White, D.J., 1995. Crustal structure and tectonics of the southeastern Canadian Cordillera, *J. Geophys. Res.*, **100**, 24255-27273.

Figure Caption

Figure 1. Bathymetric map with locations of three refraction profiles obtained during the SCREECH program (thick lines), ODP site 1277 (Leg 210; Shipboard

Scientific Party 2004), a previous refraction profile (Line 7, dashed line; Reid 1994), and selected sites of previous velocity models (gray squares; see Fig. 15 caption for references). Stars on Line 3 show OBS locations; larger, numbered stars identify OBS data illustrated in Figs 3-9. Data from other stations (small stars) are shown in Appendix A. Magnetic anomalies M0 and J-anomaly (modified from Srivastava *et al.* 2000) are shown by gray solid lines. Bathymetry is contoured every 1000 m (thin gray lines) and 200 m (gray dashed lines) for depths greater and less than 1000 m, respectively. Shaded regions indicate sediment thickness ≥ 3500 m (Louden *et al.* 2004). CA is the magnetic Collector Anomaly, which separates the Avalon (AC) and Meguma (MC) accreted terranes. The inset shows the position of the survey area relative to Newfoundland.

Figure 2. Velocity model of Line 7 (modified from Reid 1994) located in Fig. 1. Interpreted crustal layers are shown in gray. Reid (1994) interpreted the continent-ocean boundary (COB) to be at ~120 km distance. Velocities shown (in km/s) are for tops of layers.

Figure 3. (Top) Record section for the hydrophone data of OBS 4 overlain by travel times calculated from ray tracing through the velocity model. Solid lines and dashed lines are travel times for arrivals with and without picks, respectively. Time is reduced by 6.5 km/s, distance is measured from the northwestern end of the model and offsets are shot-receiver distances. Phase names are explained in Table 2. The data have been processed with bandpass filtering (4-10 Hz) and spiking deconvolution. See text for information on additional processing. (Bottom) The corresponding ray-path diagram. Continental and transitional crust are shaded (see

text). Thick lines are layer boundaries and thin lines are rays. Solid rays are observed and dashed rays are not observed. Rays that travel out of the range of the figure are not shown.

Figure 4. (Top) Record section for the vertical geophone data of OBS 9 overlain by travel times calculated from ray tracing through the velocity model. The data have been processed with bandpass filtering (4-10 Hz) and spiking deconvolution. (Middle) The corresponding ray path diagram. See Fig. 3 caption for other explanations of figure components. (Bottom) Blow-up of the area inside the rectangle in the top panel. Travel time curves are omitted.

Figure 5. (Top) Record section for the hydrophone data of OBS 10 overlain by travel times calculated from ray tracing through the velocity model. The data have been processed with bandpass filtering (4-10 Hz) and spiking deconvolution. (Bottom) The corresponding ray path diagram. Sedimentary reflection phases are omitted for clarity. See Fig. 3 caption for other explanations of figure components.

Figure 6. (Top) Record section for the hydrophone data of OBS 12 overlain by travel times calculated from ray tracing through the velocity model. “Multiple” is water-bottom multiple. The data have been processed with bandpass filtering (4-10 Hz) and spiking deconvolution. (Bottom) The corresponding ray path diagram. L2 and L3 are oceanic layers 2 and layer 3, respectively. Sed. is sediment. See Fig. 3 caption for other explanations of figure components.

Figure 7. (Top) Record section for the hydrophone data of OBS 15 overlain by travel times calculated from ray tracing through the velocity model. The data have

been processed with bandpass filtering (4-10 Hz). (Bottom) the corresponding ray path diagram. See Fig. 3 caption for other explanations of figure components.

Figure 8. (Top) Record section for the vertical geophone data of OBS 17 overlain by travel times calculated from ray tracing through the velocity model. The data have been processed with bandpass filtering (4-10 Hz). (Bottom) The corresponding ray path diagram. See Fig. 3 caption for other explanations of figure components.

Figure 9. (Top) Record section for the vertical geophone data of OBS 19 overlain by travel times calculated from ray tracing through the velocity model. The data have been processed with bandpass filtering (4-10 Hz) and spiking deconvolution. (Bottom) The corresponding ray path diagram. See Fig. 3 caption for other explanations of figure components.

Figure 10. Final P-wave velocity model and model resolution. (a) P-wave velocity model with layer boundaries in thick lines and velocities shown according to the color scale below the figure. A red line indicates the top of the interpreted basement. Velocities 5.6-8.0 km/s are contoured every 0.4 km/s (thin lines). Areas outside the ray coverage are blank. See text for detailed interpretations. Positions of magnetic anomalies M0, J and M4 are shown at the top of the figure (Srivastava *et al.* 2000). (b) Ray path diagram produced by raytracing the model with 100 rays for each phase. (c) Final velocity model plotted without vertical exaggeration. Only major layers (water, sediment, basement and mantle) are shown. (d) Velocity resolution of the model (gridded from diagonal values of the resolution matrix for all velocity nodes). Positions of OBS (yellow triangles) used in the modelling are

labelled at the top. (e) Depth resolution of the model (diagonal values of the resolution matrix for all interface nodes). Resolution is indicated by sizes of black dots inside the open circles (diameter of the black dot increases linearly with the resolution value).

Figure 11. Two models for the transitional basement (distance 385-465 km): (a) Model A – basement velocities increase smoothly to that of normal mantle or (b) Model B – a Moho exists between basement and mantle. (Top) Record sections for the hydrophone data of OBS 14 overlain by travel times calculated from ray tracing through the corresponding velocity models (see Fig. 3 caption). (Middle) Synthetic seismograms with added noise and similar bandpass filtering (4-10 Hz) for the corresponding models. (Bottom) Ray diagrams of the two models with layer boundaries (thick lines), velocity contours every 0.2 km/s for basement and mantle (thin lines), and ray paths (dotted lines). Velocities are in km/s.

Figure 12. Satellite-derived free-air gravity anomalies (Sandwell and Smith 1997). See Fig. 1 caption for explanations of other components. See Fig. 15 caption for velocity model references (AC1-AC3; MC1-MC3).

Figure 13. (Top) Comparison between observed (shaded area and dotted line; Sandwell and Smith 1997) and calculated (solid and dashed lines) gravity anomalies. The shaded area encloses variations between a track centred along Line 3 (dotted line) and two other tracks offset from Line 3 by ±40 km. (Middle) Primary and alternate gravity models used for the calculation. The primary model (solid lines) uses the velocity-model boundary depths (Fig. 10) and densities (Mg/m^3) converted from the model velocities by using the density-velocity relationship shown in Fig.

14. An exception is the bottom of the 3.15 Mg/m^3 layer, which follows the 8.0 km/s contour rather than the velocity-model boundary. An alternate model is shown in which the boundary between middle and upper crust is raised to improve the fit (dashed line). Crustal layers, including transitional basement, are shaded. (Bottom) Lithostatic pressure at the base of the primary model.

Figure 14. Density-velocity relationship used in gravity modelling of Line 3 (crosses) compared with published relationships (lines). Uncertainties are indicated by shading. Modified from Contrucci *et al.* (2004).

Figure 15. Velocity-depth models of the continental crust beneath the Grand Banks within (a) the Avalon and (b) the Meguma terranes (see Figs 1 and 12 for locations). AC1: Lithoprobe 91-2 (Marillier *et al.* 1994). AC2: Reid and Keen (1990). AC3: SCREECH-Line 1 (Funck *et al.* 2003). MC1: profile HU-1 (Todd *et al.* 1988). MC2: Reid (1988). MC3: Line 7 (Reid 1994; illustrated in Fig. 2).

Figure 16. A comparison of basement structures between a section of interpreted upper continental crust in the Newfoundland basin (Line 3, upper panel) and exhumed, serpentinized mantle on the Iberia margin (IAM-9, lower panel). The time-migrated MCS data for Line 3 (Lau *et al.*, this issue) were converted to depth using the velocity model (colour scale) presented in this paper. Time-migrated MCS data for IAM-9 (Pickup *et al.* 1996) were converted to depth using the velocity model of Dean *et al.* (2000). Distances are labelled as in the corresponding velocity models. Seaward direction is towards the right on both sections.

Figure 17. (Top) Magnetic anomaly with position of M4 as identified by Srivastava *et al.* (2000). (Bottom) Time migrated MCS section of the zone of

transitional basement on Line 3, with the velocity model (colour scale) of this paper superimposed. The original time-migrated section was coherency filtered as in Lau *et al.* (this issue) and converted to depth using the velocity model.

Figure 18. Velocity-depth models for interpreted oceanic crust at 3 locations (model distances 500, 520 and 540 km) and those of the two models proposed for the transitional basement at distance 420 km. Shaded area bounds the velocities for typical Atlantic oceanic crust (59-170 Ma; White *et al.* 1992).

Figure 19. Reconstruction of the Newfoundland basin-Iberia Abyssal Plain margins at (a) separation of continental crust, with post-rift sediment stripped off and the basement isostatically adjusted, and (b) time of J-anomaly (modified from Srivastava *et al.* (2000) for the Newfoundland basin and from Whitmarsh & Miles (1995) for the Iberia Abyssal Plain). Interpretation of the Iberia Abyssal Plain section is based on the velocity model for profile IAM-9 (Dean *et al.* 2000). The IAM-9 profile is offset ~140 km to the north of Line 3 in plate reconstructions (Srivastava *et al.* 2000). (c) Reconstruction of the Flemish Cap-Galicia Bank conjugate margins, modified from Funck *et al.* (2003). The Flemish Cap section is along SCREECH Line 1 (Fig. 1). Distance is measured from the axis of separation or spreading. PR is peridotite ridge. "S" is the detachment surface interpreted by Reston *et al.* (1996).

Appendix A – Supplementary record sections

In this appendix, record sections similar to those of Figs 3-9 are shown for OBS that are not included with the main text. This allows further assessment on constraints of the model by our data. Record sections with poor data quality (OBS 5, 8 and 18) are omitted.

Figure Caption

Figure A1. (Top) Record section for the hydrophone data of OBS 1 overlain by travel times calculated from ray tracing through the velocity model. The data have been processed with bandpass filtering (4-10 Hz). (Bottom) The corresponding ray path diagram. Note that arrivals with and without picks are both shown in solid lines. See Fig. 3 caption for other explanations of figure components.

Figure A2. (Top) Record section for the hydrophone data of OBS 2 overlain by travel times calculated from ray tracing through the velocity model. The data have been processed with bandpass filtering (4-10 Hz) and spiking deconvolution. (Bottom) The corresponding ray path diagram. See Figs 3 and A1 captions for other explanations of figure components.

Figure A3. (Top) Record section for the vertical geophone data of OBS 3 overlain by travel times calculated from ray tracing through the velocity model. The data have been processed with bandpass filtering (4-10 Hz). (Bottom) The corresponding ray path diagram. See Fig. 3 and Fig. A1 captions for other explanations of figure components.

Figure A4. (Top) Record section for the hydrophone data of OBS 26 overlain by travel times calculated from ray tracing through the velocity model. The data have been processed with bandpass filtering (4-10 Hz). (Bottom) The corresponding ray path diagram. See Fig. 3 and Fig. A1 captions for other explanations of figure components.

Figure A5. (Top) Record section for the hydrophone data of OBS 6 overlain by travel times calculated from ray tracing through the velocity model. The data have been processed with bandpass filtering (4-10 Hz) and spiking deconvolution. (Bottom) The corresponding ray path diagram. FR – floating reflector. See Fig. 3 and Fig. A1 captions for other explanations of figure components.

Figure A6. (Top) Record section for the hydrophone data of OBS 25 overlain by travel times calculated from ray tracing through the velocity model. The data have been processed with bandpass filtering (4-10 Hz). (Bottom) The corresponding ray path diagram. See Fig. 3 and Fig. A1 captions for other explanations of figure components.

Figure A7. (Top) Record section for the hydrophone data of OBS 7 overlain by travel times calculated from ray tracing through the velocity model. The data have been processed with bandpass filtering (4-10 Hz). (Bottom) The corresponding ray path diagram. See Fig. 3 and Fig. A1 captions for other explanations of figure components.

Figure A8. (Top) Record section for the vertical geophone data of OBS 9 overlain by travel times calculated from ray tracing through the velocity model. Unlike other record sections, this section is plotted with a reduction velocity of 3

km/s to show major sedimentary phases. The data have been processed with bandpass filtering (4-20 Hz). (Bottom) The corresponding ray path diagram. See Fig. 3 and Fig. A1 captions for other explanations of figure components.

Figure A9. (Top) Record section for the vertical geophone data of OBS 10 overlain by travel times calculated from ray tracing through the velocity model. The data have been processed with bandpass filtering (4-10 Hz) and spiking deconvolution. (Bottom) The corresponding ray path diagram. See Fig. 3 and Fig. A1 captions for other explanations of figure components.

Figure A10. (Top) Record section for the hydrophone data of OBS 11 overlain by travel times calculated from ray tracing through the velocity model. The data have been processed with bandpass filtering (4-10 Hz). (Bottom) The corresponding ray path diagram. See Fig. 3 and Fig. A1 captions for other explanations of figure components.

Figure A11. (Top) Record section for the hydrophone data of OBS 13 overlain by travel times calculated from ray tracing through the velocity model. The data have been processed with bandpass filtering (4-10 Hz). (Bottom) The corresponding ray path diagram. See Fig. 3 and Fig. A1 captions for other explanations of figure components.

Figure A12. (Top) Record section for the hydrophone data of OBS 14 overlain by travel times calculated from ray tracing through the velocity model. The data have been processed with bandpass filtering (4-10 Hz). (Bottom) The corresponding ray path diagram. See Fig. 3 and Fig. A1 captions for other explanations of figure components.

Figure A13. (Top) Record section for the hydrophone data of OBS 16 overlain by travel times calculated from ray tracing through the velocity model. The data have been processed with bandpass filtering (4-10 Hz) and spiking deconvolution. (Bottom) The corresponding ray path diagram. See Fig. 3 and Fig. A1 captions for other explanations of figure components.

Figure A14. (Top) Record section for the hydrophone data of OBS 22 overlain by travel times calculated from ray tracing through the velocity model. The data have been processed with bandpass filtering (4-15 Hz). (Bottom) The corresponding ray path diagram. See Fig. 3 and Fig. A1 captions for other explanations of figure components.

Figure A15. (Top) Record section for the hydrophone data of OBS 23 overlain by travel times calculated from ray tracing through the velocity model. The data have been processed with bandpass filtering (4-15 Hz). (Bottom) The corresponding ray path diagram. See Fig. 3 and Fig. A1 captions for other explanations of figure components.

with Line 3. Crustal boundaries with a question mark are extrapolations (see text). M0 and J are magnetic anomalies (see Fig. 1 caption). See text for explanations of crustal zones T1 to O2 and large basement high. L: prominent landward dipping reflections where the length of line shows the seaward and landward limit of the reflection on the profile.

Table

Table 1. Ocean Bottom Seismometer configurations

OBS #	Latitude (°)	Longitude (°)	Water Depth (m)	Sensors	Sampling rate (ms)	Error (m)	Drifted distance (m)
1	46.7323	-50.5090	108	H + G	5.734	-	0
2	46.4654	-49.9823	76	H + G	5.734	-	0
3	46.1959	-49.4594	71	H + G	7.168	-	0
4	45.9257	-48.9430	71	H + G	5.734	-	0
5	45.6510	-48.4310	128	H	5.000	-	0
26	45.5887	-48.3133	417	H	5.000	-	0
6	45.5238	-48.1997	1163	H	5.000	11	179
25	45.4608	-48.0801	1447	H + G	7.168	7	100
7	45.3981	-47.9650	1695	H	5.000	18	62
8	45.2716	-47.7311	2480	H	5.000	6	145
9	45.1421	-47.5017	3121	H + G	5.734	24	123
10	45.0136	-47.2724	3580	H + G	7.168	80	46
11	44.8841	-47.0432	3651	H + G	7.168	38	152
12	44.7881	-46.8743	3675	H	5.000	36	117
13	44.6917	-46.7054	3838	H	5.000	58	231
14	44.5965	-46.5398	3850	H	5.000	10	176
15	44.5025	-46.3718	3820	H	5.000	7	206
16	44.4090	-46.2036	3924	H	5.000	11	652
17	44.3085	-46.0449	4017	H + G	7.168	32	227
18	44.2117	-45.8802	3953	H + G	7.168	53	193
19	44.1352	-45.7508	4096	H + G	7.168	78	218
20	No data recorded						
21							
22	43.9048	-45.3654	4559	H	5.000	17	331
23	43.8351	-45.2280	4617	H	5.000	20	1076

H = hydrophone

H + G = hydrophone and three-component geophones

Error = RMS errors in range between relocated OBS positions and shot positions; "-" means no relocation neccessary

Table 2. Glossary of seismic phases

Phase	Description
Direct	Direct wave through the water
P_{Sn}	P-wave refracted phase through the n^{th} post-rift sedimentary layer from the top
$P_{Sn}P$	P-wave reflected phase from the bottom of the n^{th} post-rift sedimentary layer from the top
$P_{S4}P$	P-wave reflected phase coincident with the "U" reflection for OBS 10-15
P_{SYn}	P-wave refracted phase through the n^{th} Syn-rift sedimentary layer from the top
P_BP	P-wave reflected phase from the basement top
P_{C1} /P_{C2}/P_{C3}	P-wave refracted phase through the upper/middle/lower continental crust
$P_{C1}P$/ $P_{C2}P$	P-wave reflected phase from the bottom of the upper/middle continental crust
P_{L2}/P_{L3}	P-wave refracted phase through the oceanic layer-2/3.
$P_{L2}P$	P-wave reflected phase from the bottom of the up oceanic layer-2
P_mP	P-wave Moho reflection or reflection at the crust-mantle boundary
P_{T1}	P-wave refracted phase through exhumed highly serpentinized mantle or transitional crust 1
P_{T2}	P-wave refracted phase through moderately serpentinized mantle or transitional crust 2
P_{n1}	P-wave refracted phase through slightly serpentinized mantle or low velocity mantle layer
P_{n2}	P-wave refracted phase through unaltered mantle

Table 3. Error analysis statistic: number of observations (n), RMS misfit between calculated and observed travel times (t_{rms}) and normalized (χ^2)

Phase	n	t_{rms} (s)	χ^2
Direct	2534	0.050	2.514
P_{S1}	9	0.039	1.075
$P_{S1}P$	221	0.024	0.822
P_{S2}	555	0.022	0.574
$P_{S2}P$	569	0.019	0.727
P_{S3}	702	0.030	0.796
$P_{S3}P$	777	0.020	0.679
P_{S4}	388	0.054	0.970
$P_{S4}P$	362	0.020	0.764
P_{S5}	586	0.039	0.513
P_{SY1}	134	0.031	0.828
P_{SY2}	254	0.057	1.420
P_BP	217	0.065	0.912
P_{C1}	2610	0.163	2.403
$P_{C1}P$	336	0.113	3.559
P_{C2}	1665	0.203	2.139
$P_{C2}P$	1254	0.178	1.911
P_{C3}	616	0.152	1.163
P_{L2}	153	0.033	0.752
$P_{L2}P$	59	0.044	0.712
P_{L3}	234	0.053	1.753
P_mP	2990	0.249	1.512
P_{T1}	25	0.077	4.227
P_{T2}	197	0.071	2.360
P_{n1}	3996	0.083	1.679
P_{n2}	2165	0.246	1.905
All	23608	0.153	1.837

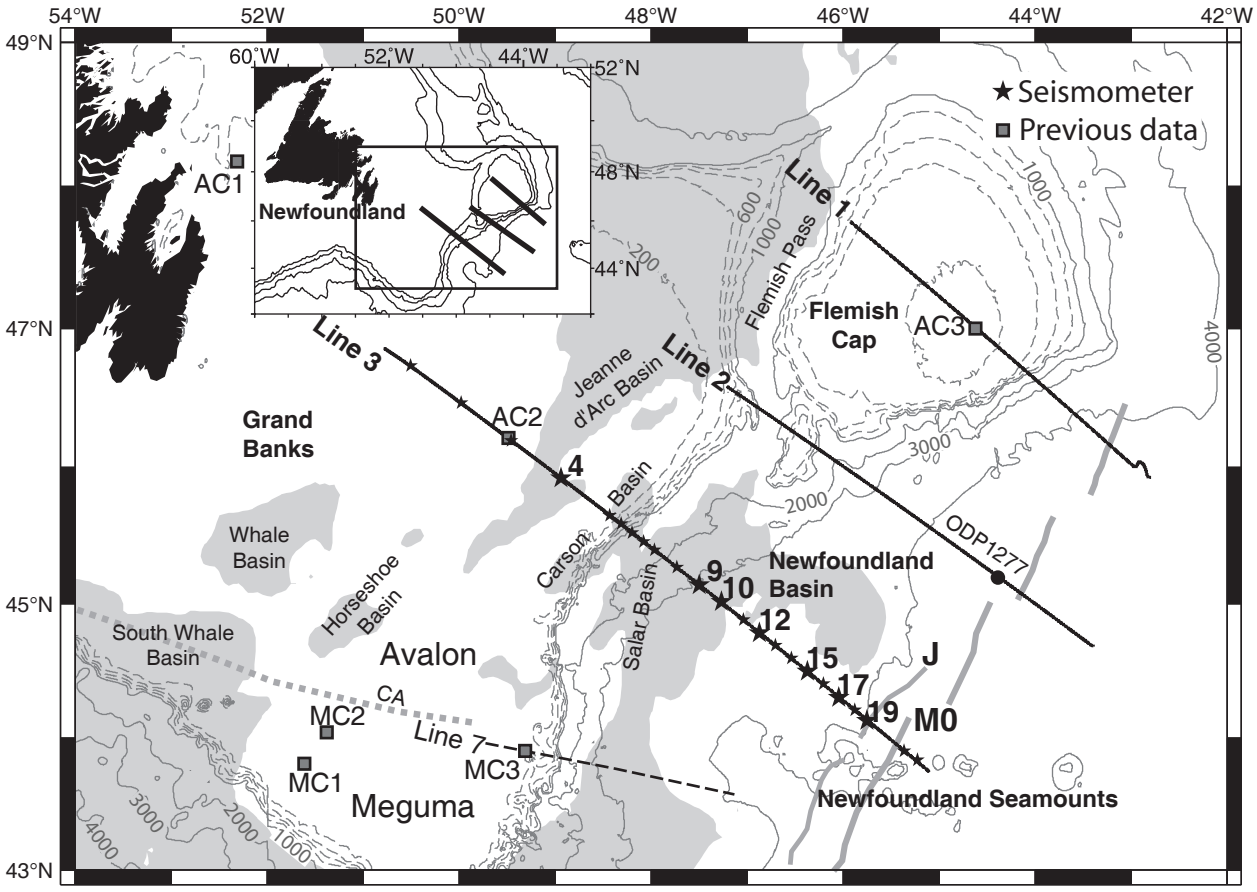
54°W
52W
50°W
48°W
46°W
44°W
42°W
49°N
47°N
45°N
43°N
60°W
52°W
44°W
52°N
48°N
44°N
Newfoundland
★Seismometer
Previous data
AC1
AC2
AC3
Line 1
Line 2
Line 3
Flemish Pass
Flemish Cap
Jeanne d'Arc Basin
Grand Banks
Whale Basin
Horseshoe Basin
South Whale Basin
Avalon
Carson Basin
Salar Basin
Newfoundland Basin
ODP1277
CA
Line 7
MC1
MC2
MC3
Meguma
Newfoundland Seamounts
4
9
10
12
15
17
19
J
M0
200
600
1000
2000
3000
4000

Figure 1.

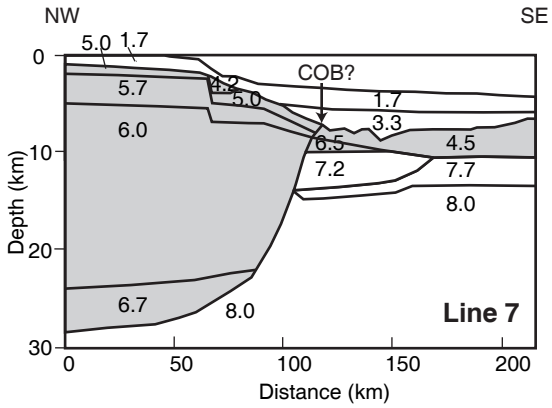
NW
SE
5.0
1.7
0
COB?
5.7
4.2
5.0
1.7
3.3
6.0
6.5
4.5
10
7.2
7.7
8.0
Depth (km)
20
6.7
8.0
Line 7
30
0
50
100
150
200
Distance (km)

Figure 2.

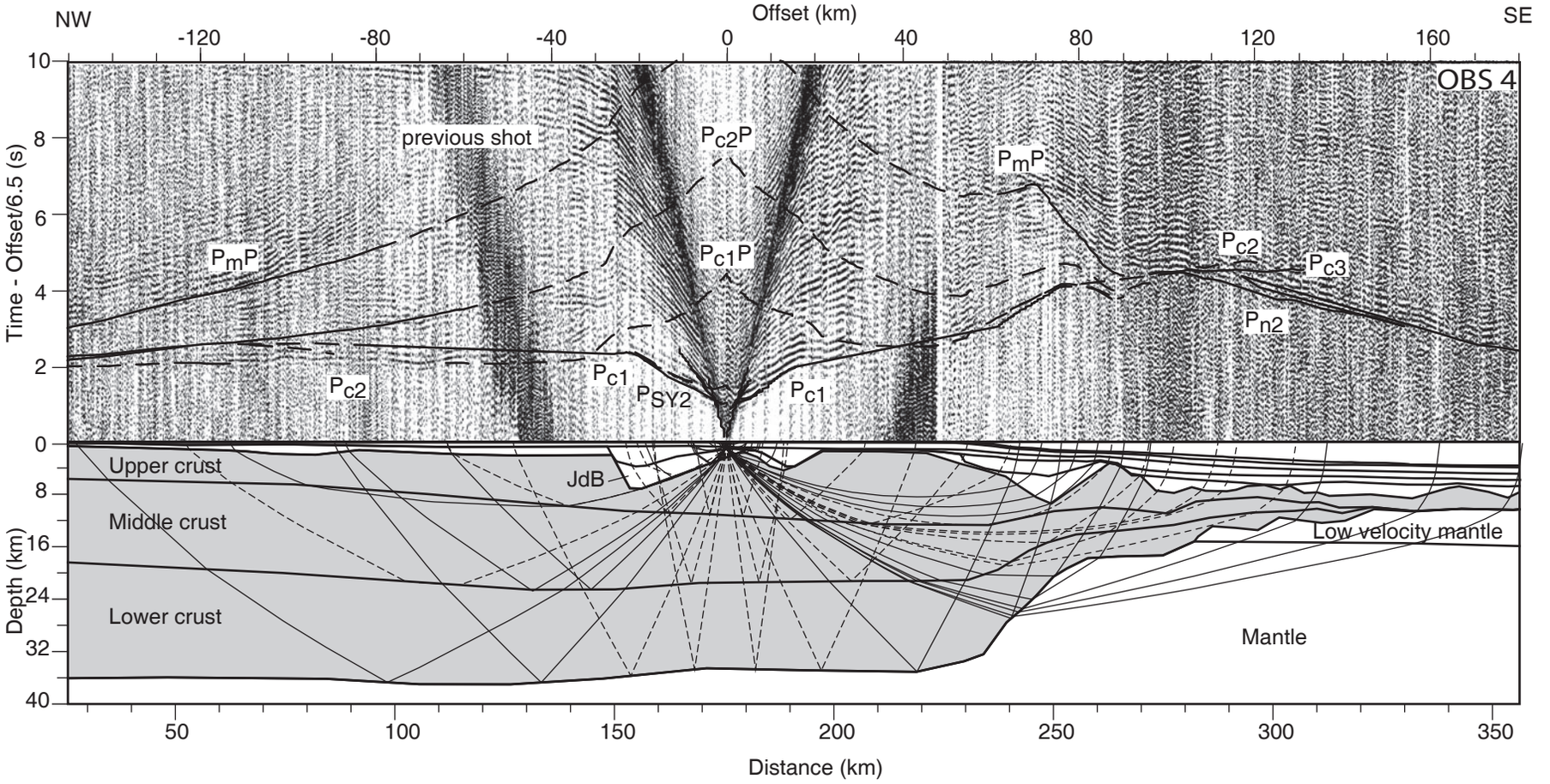
NW
Offset (km)
SE
-120
-80
-40
0
40
80
120
160
OBS 4
previous shot
$P_{c2}P$
P_mP
$P_{c1}P$
P_{c2}
P_{c3}
P_{n2}
P_{c1}
P_{SY2}
Time - Offset/6.5 (s)
10
8
6
4
2
0
Upper crust
JdB
Middle crust
Low velocity mantle
Lower crust
Mantle
Depth (km)
8
16
24
32
40
50
100
150
200
250
300
350
Distance (km)

Figure 3.

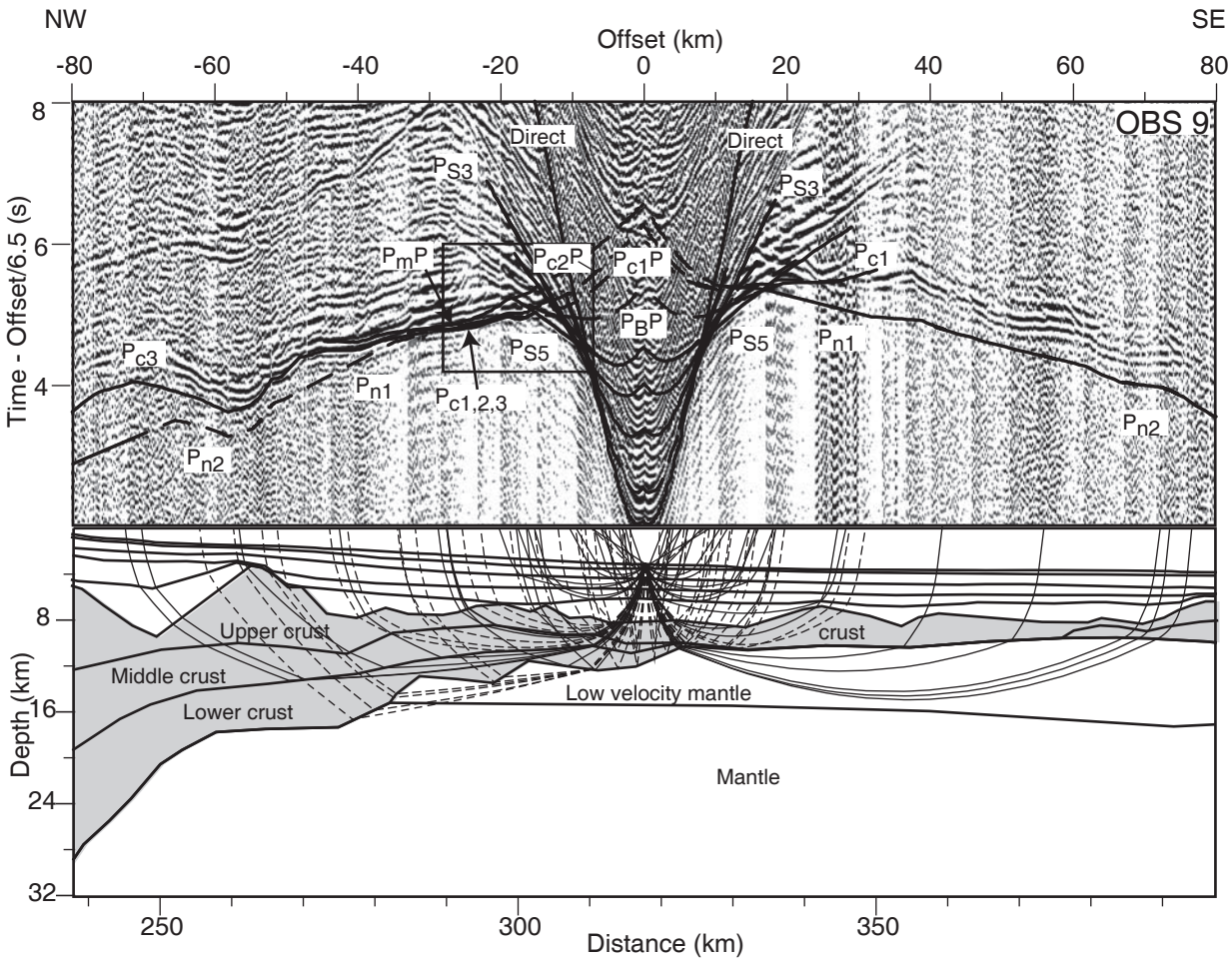
NW
SE
Offset (km)
-80
-60
-40
-20
0
20
40
60
80
OBS 9
Direct
Direct
P_{S3}
P_{S3}
P_mP
$P_{c2}P$
$P_{c1}P$
P_{c1}
P_BP
P_{S5}
P_{S5}
P_{n1}
P_{c3}
P_{n1}
$P_{c1,2,3}$
P_{n2}
P_{n2}
Time - Offset/6.5 (s)
8
6
4
Upper crust
Middle crust
Lower crust
crust
Low velocity mantle
Mantle
Depth (km)
8
16
24
32
250
300
350
Distance (km)

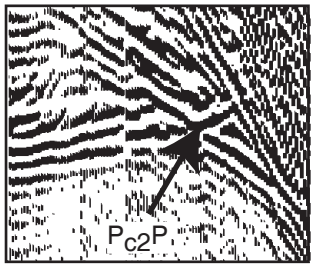
$P_{c2}P$

Figure 4.

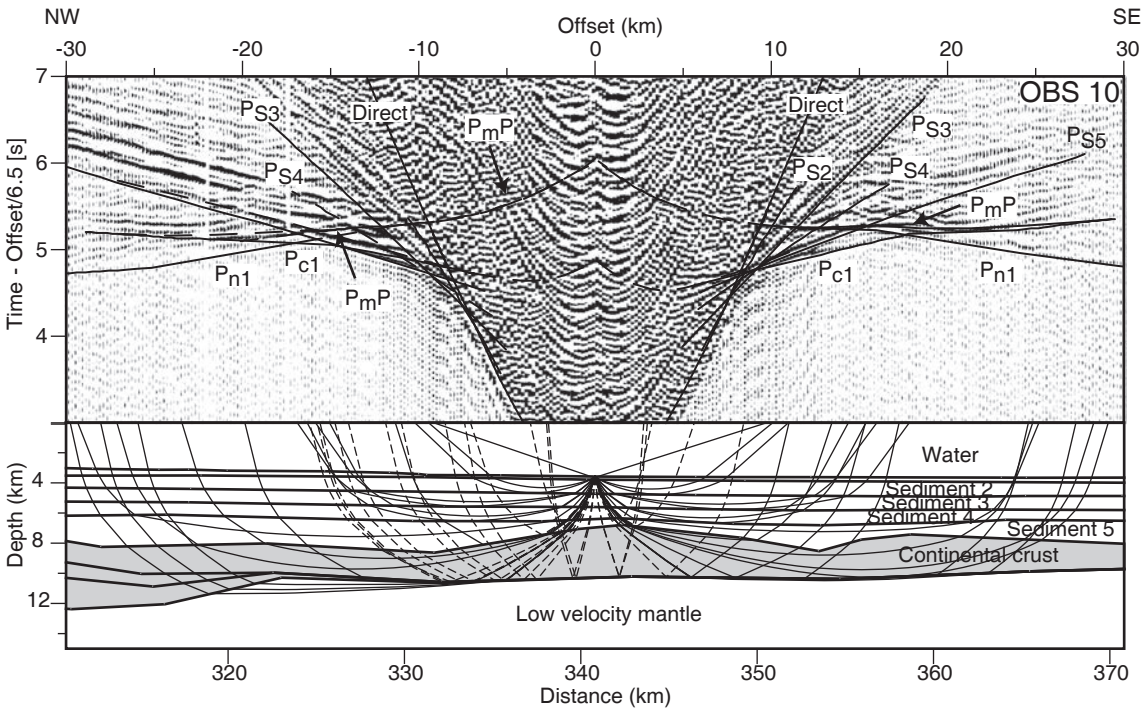
NW
SE
Offset (km)
-30
-20
-10
0
10
20
30
OBS 10
Direct
Direct
P_{S3}
P_{mP}
P_{S4}
P_{S2}
P_{S3}
P_{S5}
P_{S4}
P_{mP}
P_{n1}
P_{c1}
P_{mP}
P_{c1}
P_{n1}
Time - Offset/6.5 [s]
7
6
5
4
Depth (km)
4
8
12
Water
Sediment 2
Sediment 3
Sediment 4
Sediment 5
Continental crust
Low velocity mantle
320
330
340
350
360
370
Distance (km)

Figure 5

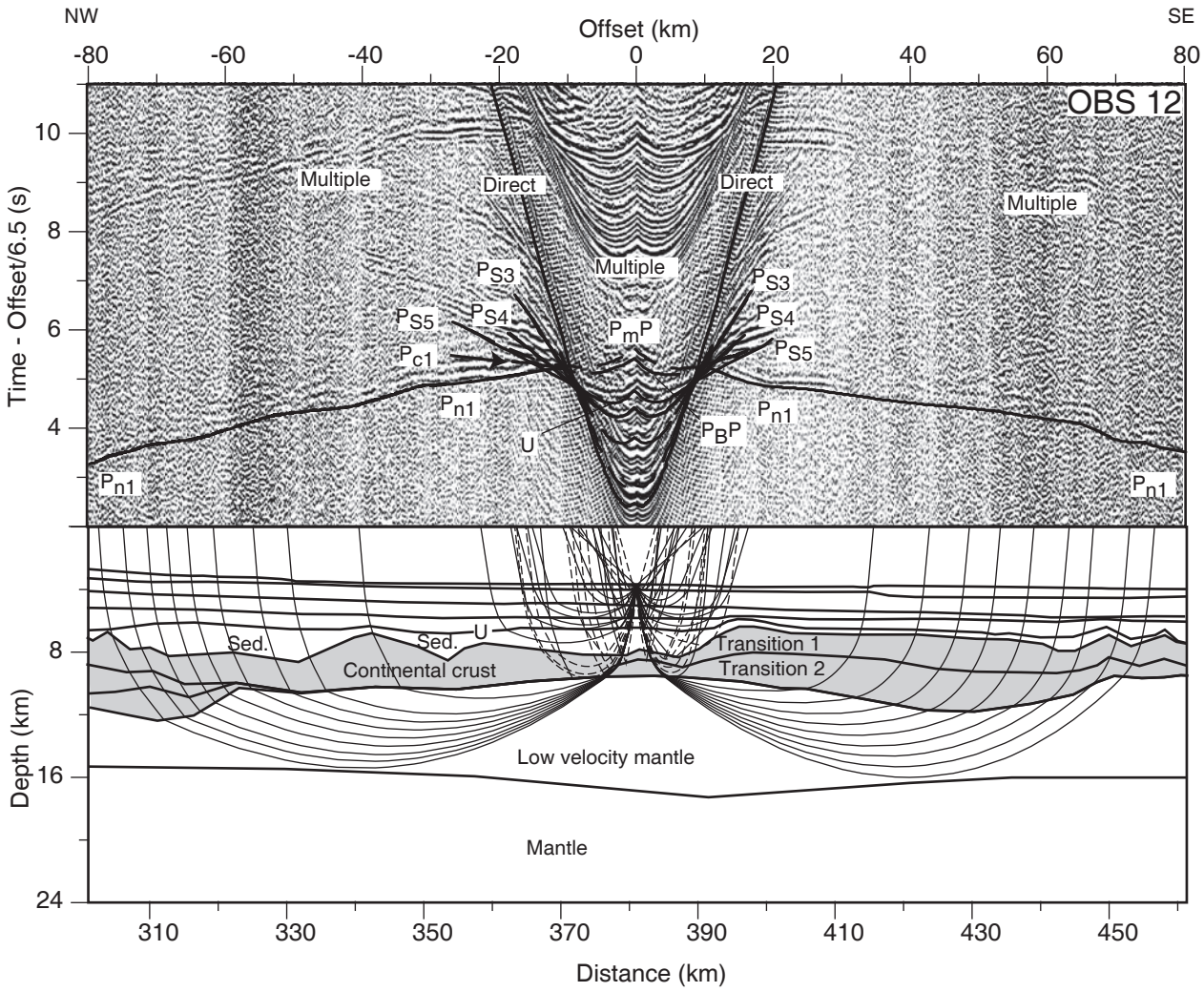
NW
SE
Offset (km)
-80
-60
-40
-20
0
20
40
60
80
OBS 12
Time - Offset/6.5 (s)
10
8
6
4
Multiple
Direct
Direct
Multiple
Multiple
P_{S3}
P_{S5}
P_{S4}
P_{c1}
P_{n1}
P_mP
U
P_BP
P_{S3}
P_{S4}
P_{S5}
P_{n1}
P_{n1}
P_{n1}
Sed.
Sed.
U
Continental crust
Transition 1
Transition 2
Low velocity mantle
Mantle
Depth (km)
8
16
24
310
330
350
370
390
410
430
450
Distance (km)

Figure 6.

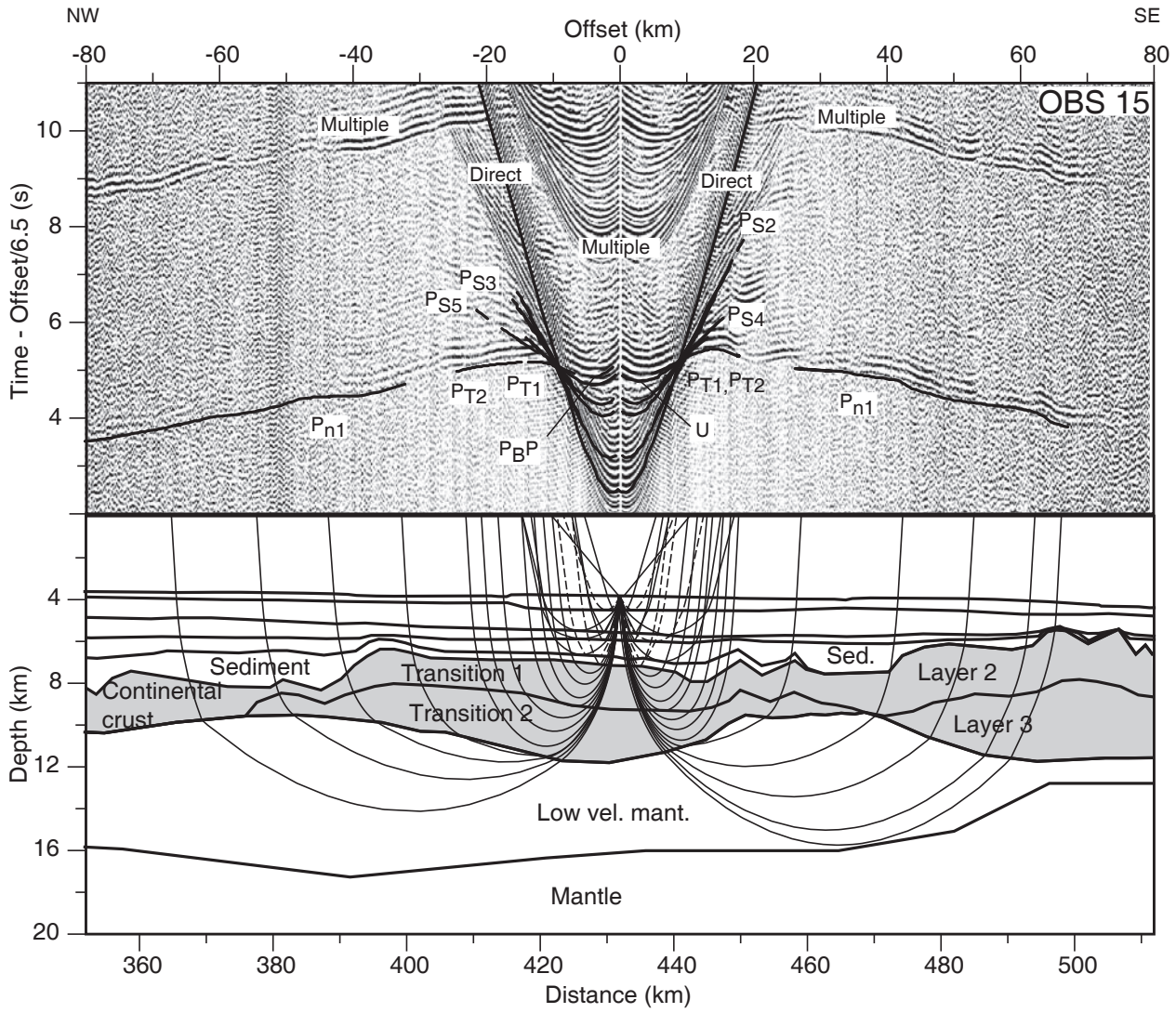
NW
SE
Offset (km)
-80
-60
-40
-20
0
20
40
60
80
OBS 15
Multiple
Multiple
Direct
Direct
Multiple
P_{S2}
P_{S3}
P_{S5}
P_{S4}
P_{T2}
P_{T1}
P_{T1}, P_{T2}
P_{n1}
P_{n1}
P_BP
U
Time - Offset/6.5 (s)
10
8
6
4
4
8
12
16
20
Depth (km)
Sediment
Continental crust
Transition 1
Transition 2
Sed.
Layer 2
Layer 3
Low vel. mant.
Mantle
360
380
400
420
440
460
480
500
Distance (km)

Figure 7.

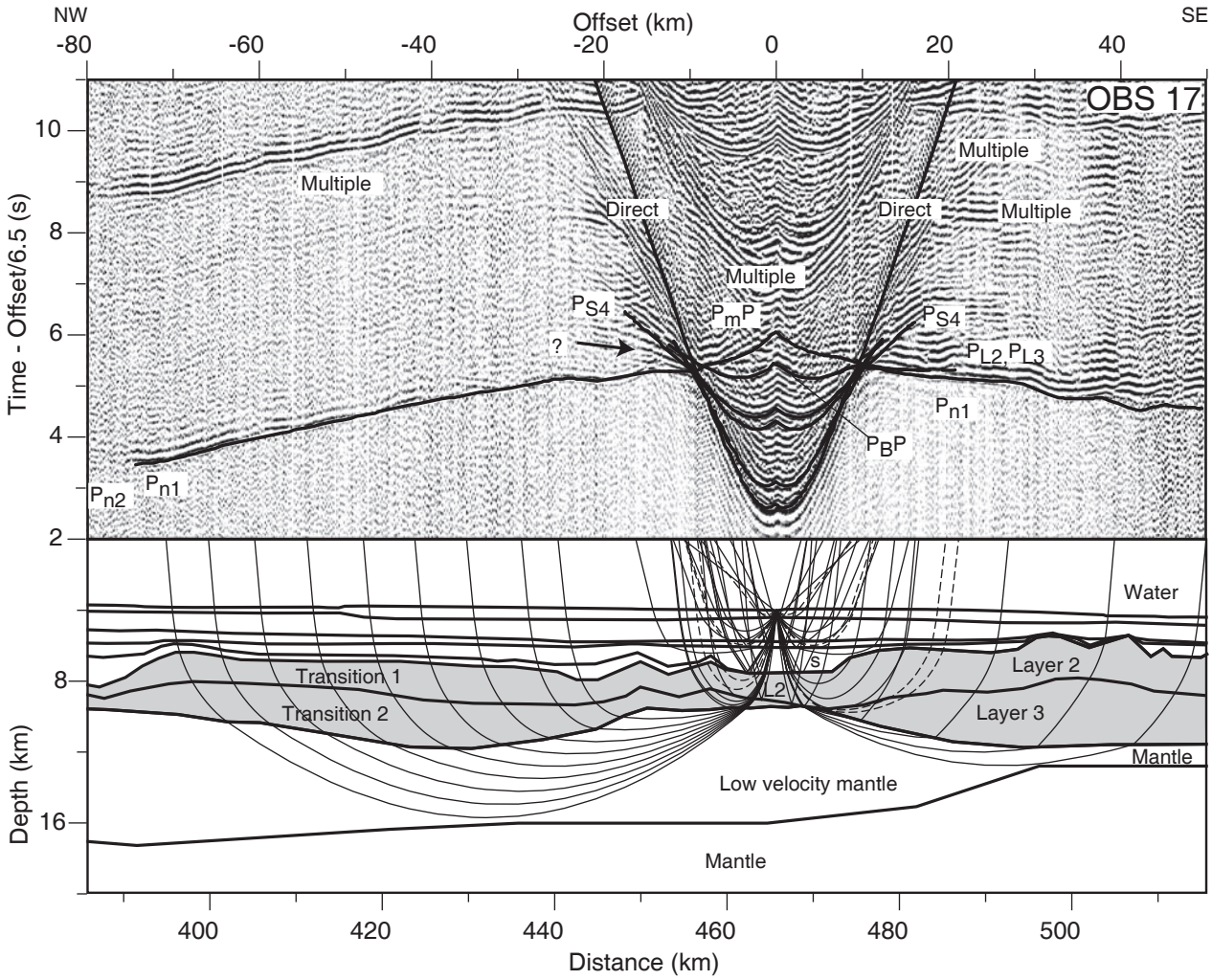
NW
SE
Offset (km)
-80
-60
-40
-20
0
20
40
OBS 17
Multiple
Direct
Direct
Multiple
Multiple
Multiple
P_{S4}
P_mP
P_{S4}
?
P_{L2}, P_{L3}
P_{n1}
P_BP
P_{n2}
P_{n1}
Time - Offset/6.5 (s)
10
8
6
4
2
Water
Transition 1
Transition 2
s
L2
Layer 2
Layer 3
Mantle
Low velocity mantle
Mantle
Depth (km)
8
16
400
420
440
460
480
500
Distance (km)

Figure 8.

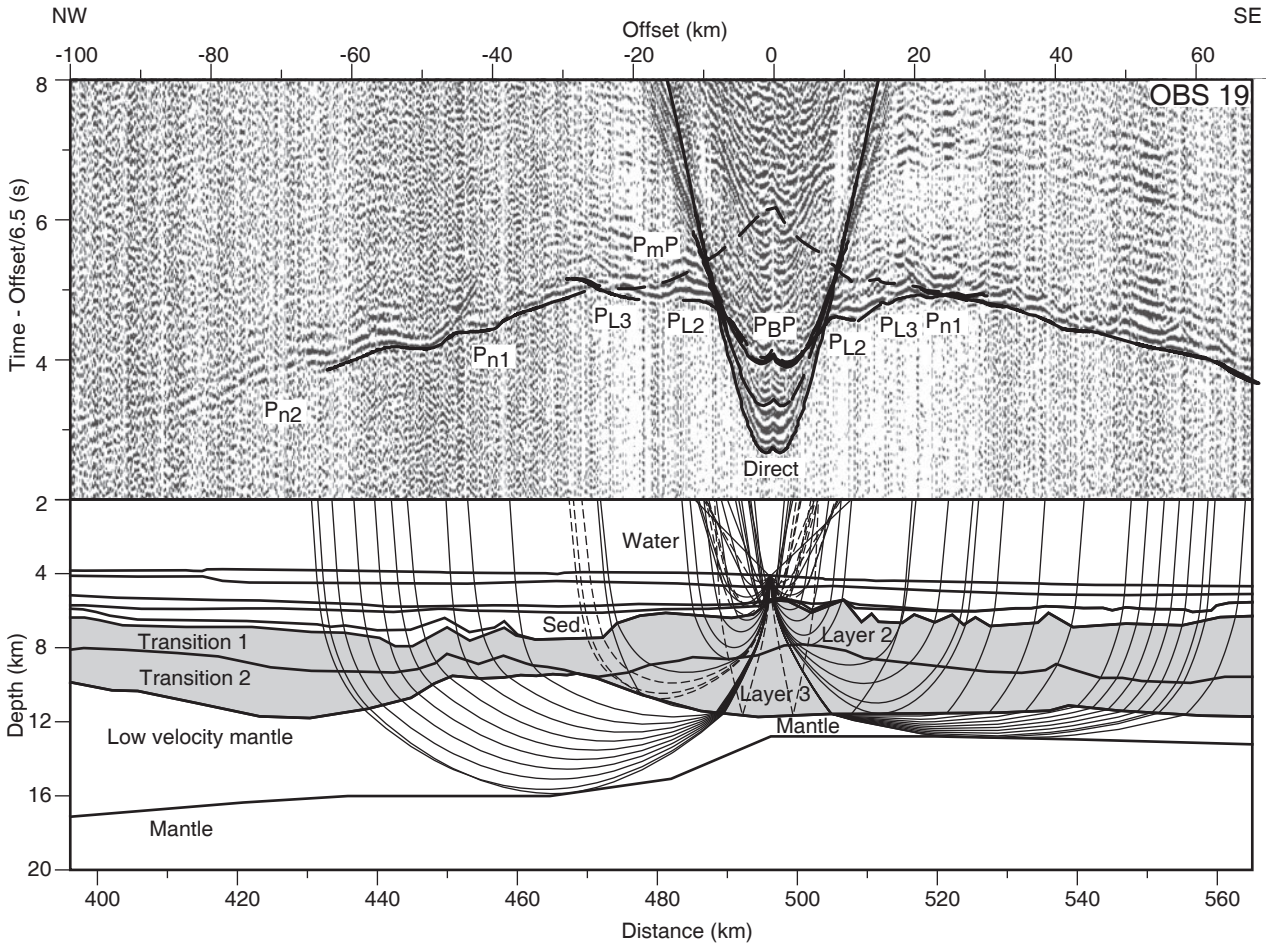
NW
SE
Offset (km)
-100
-80
-60
-40
-20
0
20
40
60
OBS 19
Time - Offset/6.5 (s)
8
6
4
2
P_{mP}
P_{L3}
P_{L2}
P_BP
P_{L2}
P_{L3}
P_{n1}
P_{n1}
P_{n2}
Direct
Water
Sed
Transition 1
Transition 2
Low velocity mantle
Mantle
Layer 2
Layer 3
Mantle
Depth (km)
2
4
8
12
16
20
400
420
440
460
480
500
520
540
560
Distance (km)

Figure 9.

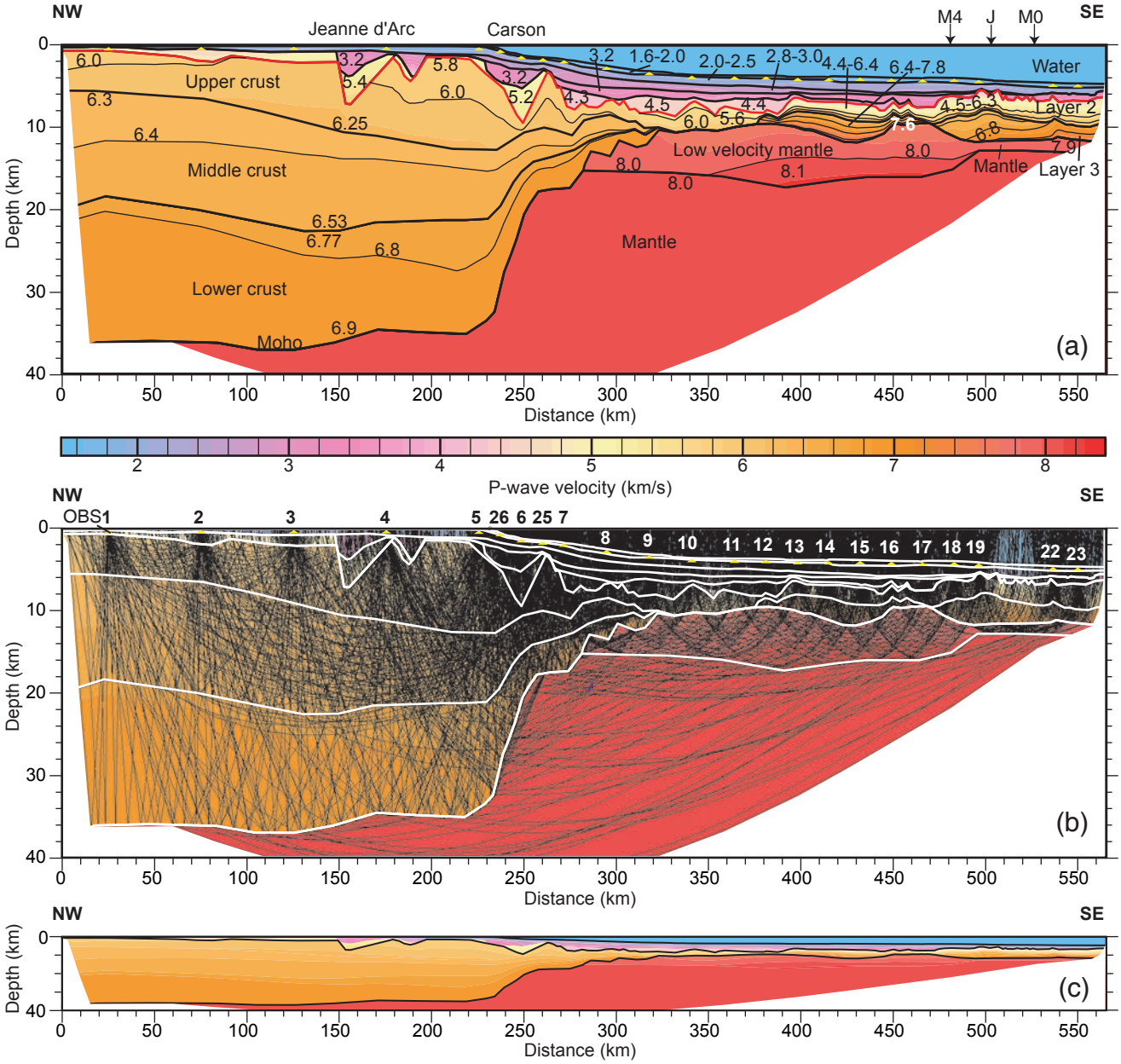
NW
SE
Jeanne d'Arc
Carson
M4
J
M0
Water
Layer 2
Layer 3
Upper crust
Middle crust
Lower crust
Low velocity mantle
Mantle
Moho
6.0
6.3
6.4
6.25
6.53
6.77
6.8
6.9
3.2
5.4
5.8
6.0
5.2
4.3
4.5
4.4
6.0
5.6
1.6-2.0
2.0-2.5
2.8-3.0
4.4-6.4
6.4-7.8
4.5-6.3
7.6
6.8
7.9
8.0
8.1
Depth (km)
Distance (km)
(a)
P-wave velocity (km/s)
OBS
1 2 3 4 5 26 6 25 7 8 9 10 11 12 13 14 15 16 17 18 19 22 23
(b)
(c)

Figure 10.

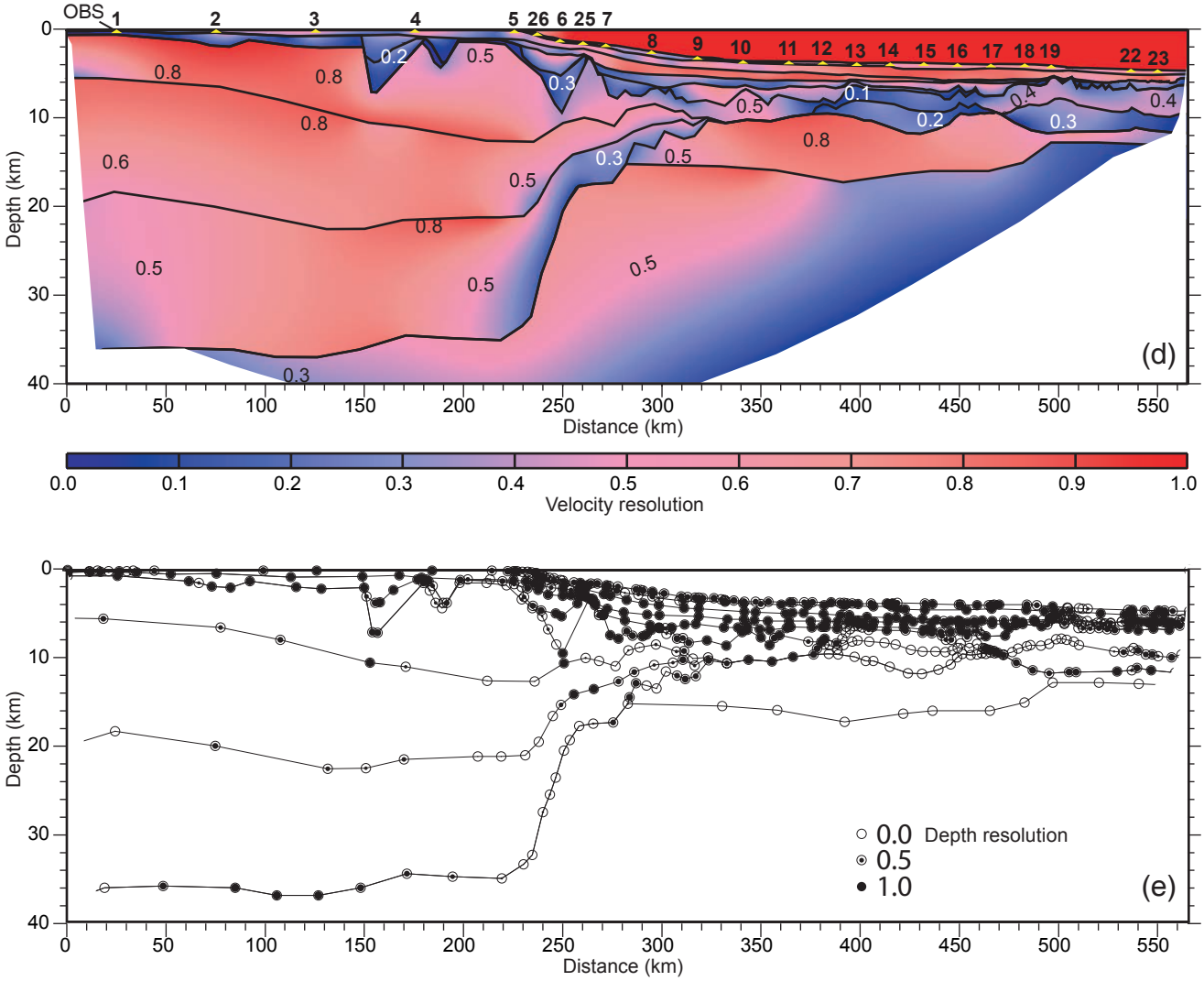

Figure 10. (continued)

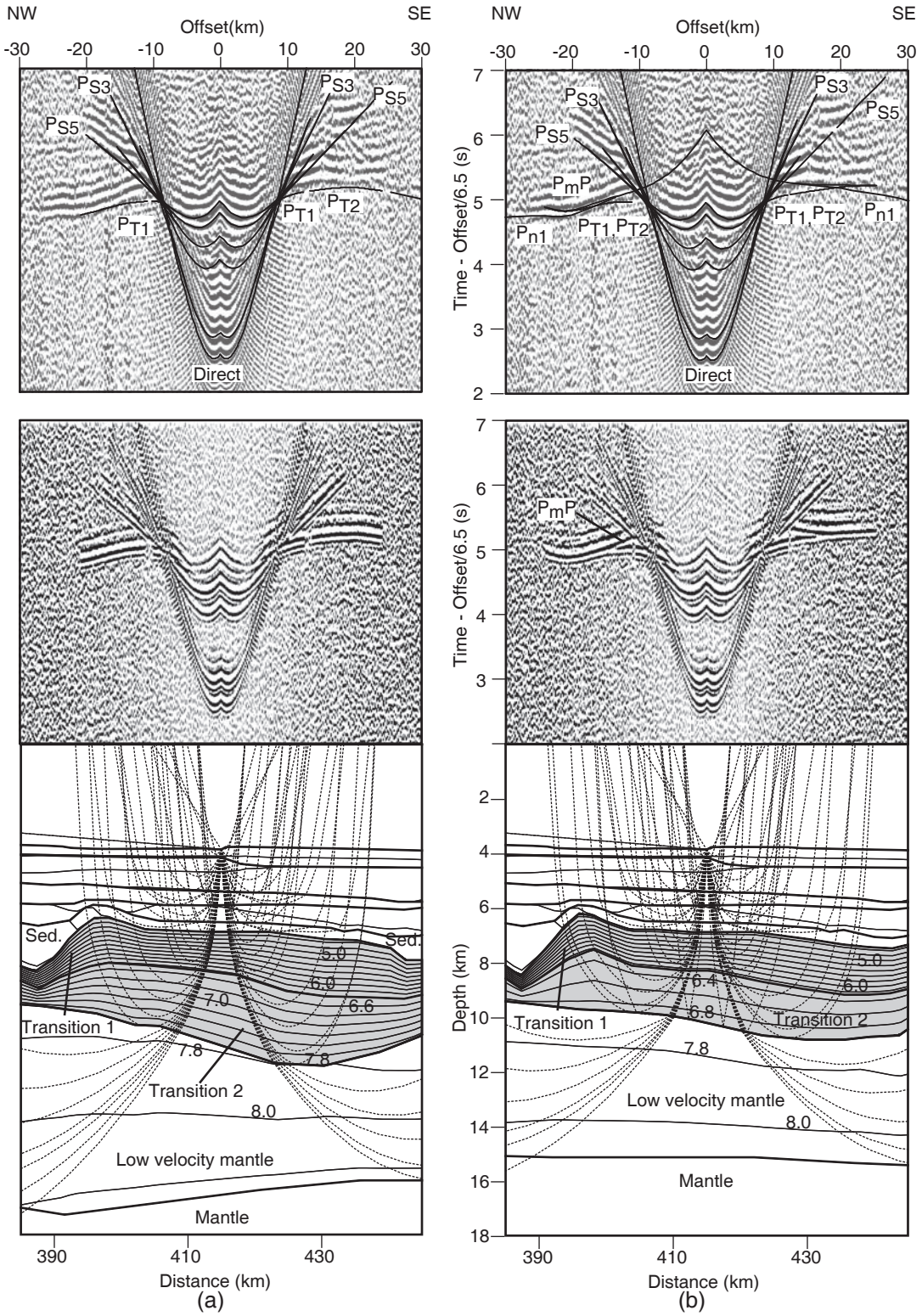
NW
SE
Offset(km)
-30
-20
-10
0
10
20
30
PS3
PS5
PT1
PT2
Direct
Time - Offset/6.5 (s)
PmP
Pn1
Sed.
5.0
6.0
6.4
6.6
6.8
7.0
7.8
Transition 1
Transition 2
8.0
Low velocity mantle
Mantle
Depth (km)
390
410
430
Distance (km)
(a)
(b)

Figure 11.

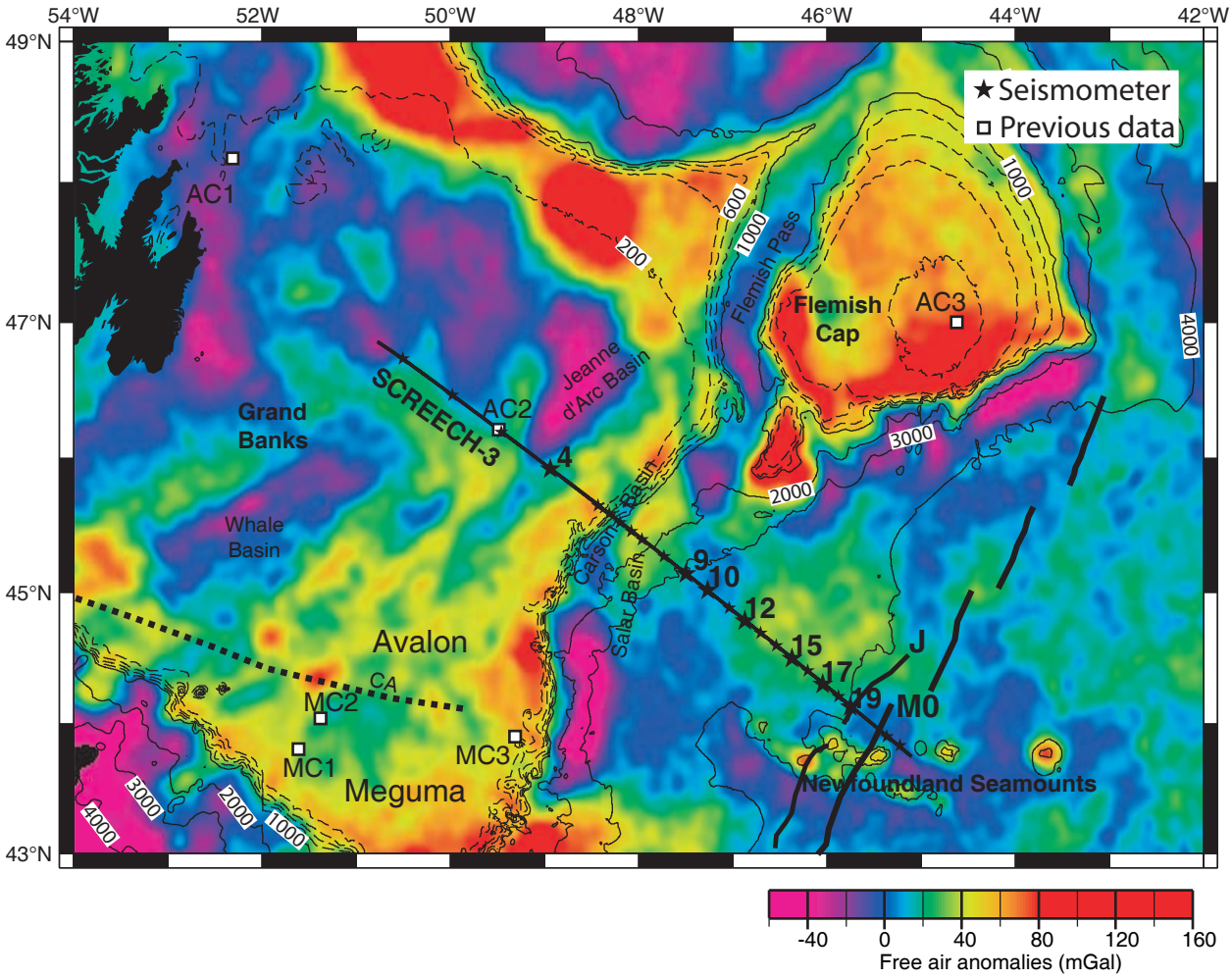
54°W
52W
50°W
48°W
46°W
44°W
42°W
49°N
47°N
45°N
43°N
★Seismometer
□ Previous data
AC1
AC2
AC3
SCREECH-3
4
Grand Banks
Whale Basin
Jeanne d'Arc Basin
Flemish Pass
Flemish Cap
Carson Basin
Salar Basin
9
10
12
15
17
19
J
M0
Avalon
CA
MC1
MC2
MC3
Meguma
Newfoundland Seamounts
200
600
1000
2000
3000
4000
-40
0
40
80
120
160
Free air anomalies (mGal)

Figure 12.

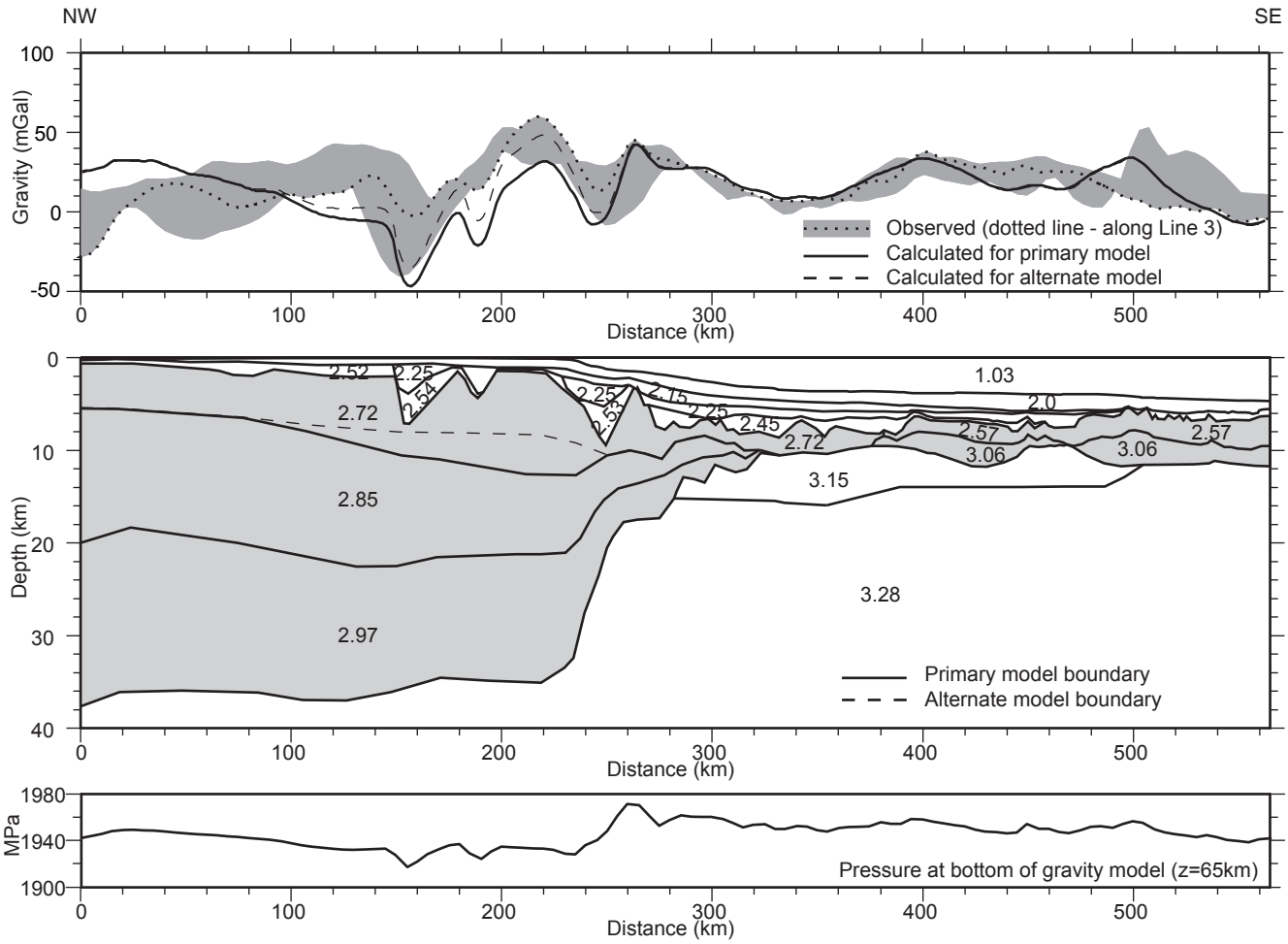
NW
SE
Gravity (mGal)
Observed (dotted line - along Line 3)
Calculated for primary model
Calculated for alternate model
Distance (km)
Depth (km)
1.03
2.0
2.52
2.25
2.54
2.72
2.15
2.45
2.57
3.06
3.15
2.85
3.28
2.97
Primary model boundary
Alternate model boundary
MPa
Pressure at bottom of gravity model (z=65km)

Figure 13.

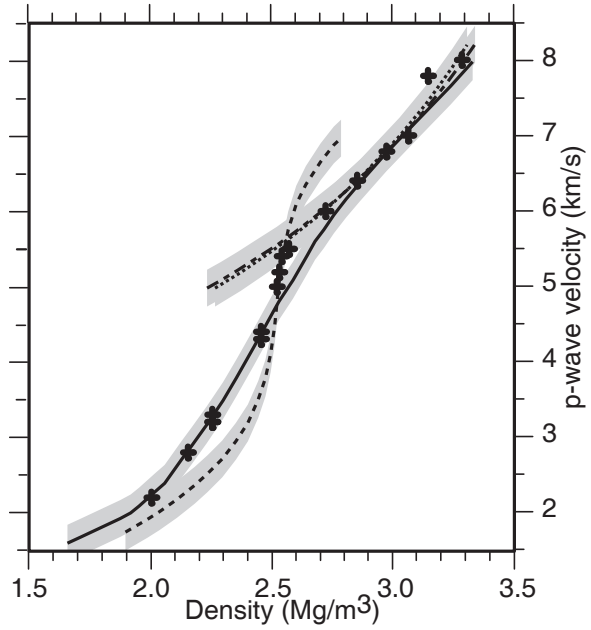
8
7
6
5
4
3
2
p-wave velocity (km/s)
1.5
2.0
2.5
3.0
3.5
Density (Mg/m3)
Christensen & Mooney (1995) 10 km depth
Christensen & Mooney (1995) 20 km depth
Ludwig et al. (1970)
Hughes et al. (1998)
Line 3

Figure 14

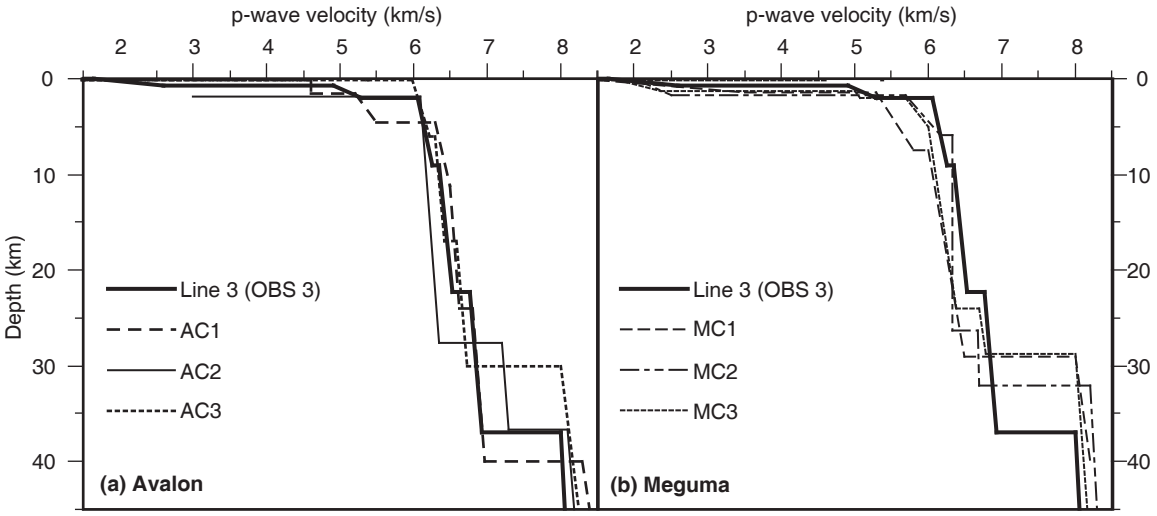
p-wave velocity (km/s)
2
3
4
5
6
7
8
0
10
20
30
40
Depth (km)
Line 3 (OBS 3)
AC1
AC2
AC3
(a) Avalon
p-wave velocity (km/s)
Line 3 (OBS 3)
MC1
MC2
MC3
(b) Meguma

Figure 15.

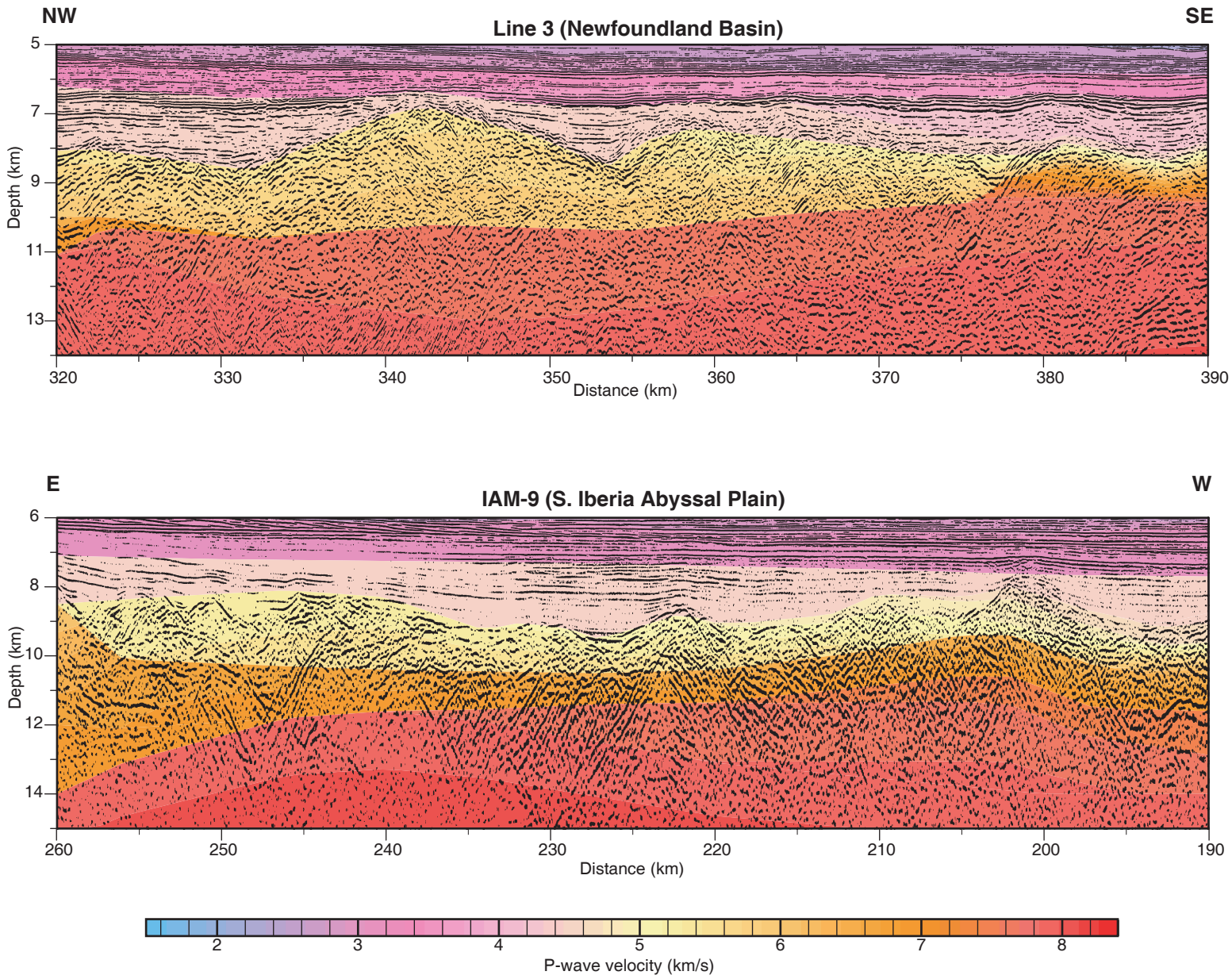
NW
Line 3 (Newfoundland Basin)
SE
Depth (km)
5
7
9
11
13
320
330
340
350
360
370
380
390
Distance (km)
E
IAM-9 (S. Iberia Abyssal Plain)
W
Depth (km)
6
8
10
12
14
260
250
240
230
220
210
200
190
Distance (km)
2
3
4
5
6
7
8
P-wave velocity (km/s)

Figure 16

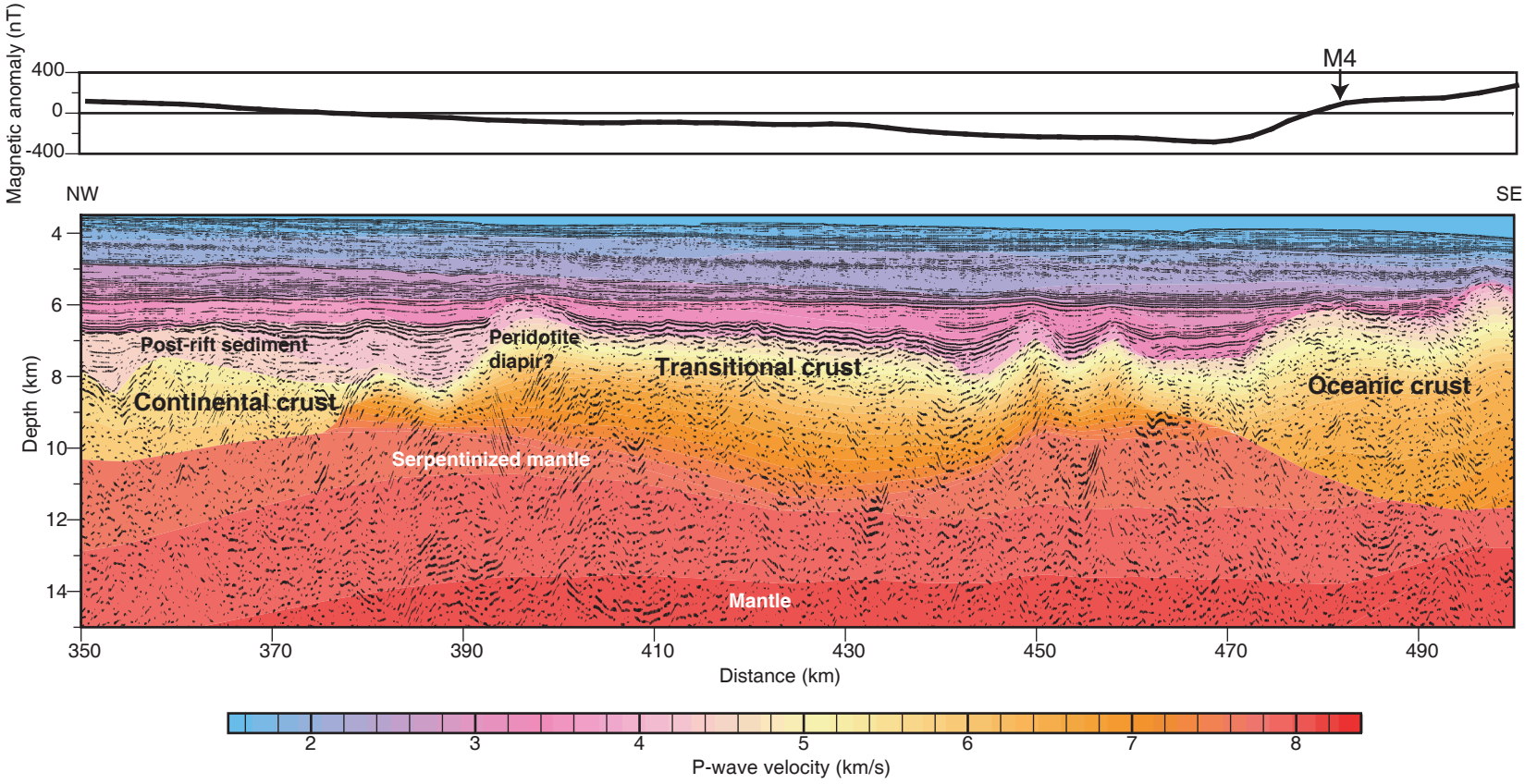
Magnetic anomaly (nT)
400
0
-400
M4
NW
SE
Depth (km)
4
6
8
10
12
14
Post-rift sediment
Peridotite diapir?
Transitional crust
Oceanic crust
Continental crust
Serpentinized mantle
Mantle
350
370
390
410
430
450
470
490
Distance (km)
2
3
4
5
6
7
8
P-wave velocity (km/s)

Figure 17.

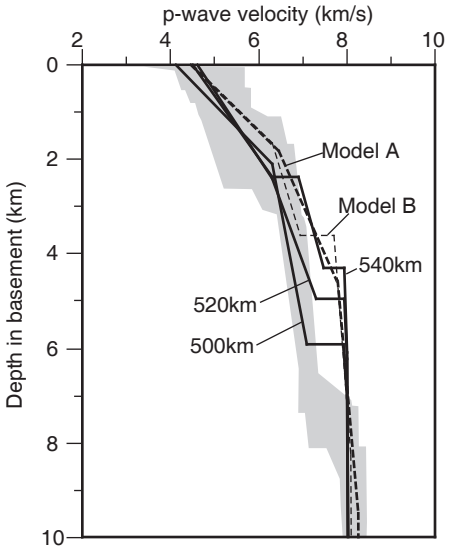
p-wave velocity (km/s)
2
4
6
8
10
0
2
4
6
8
10
Depth in basement (km)
Model A
Model B
540km
520km
500km

Figure 18

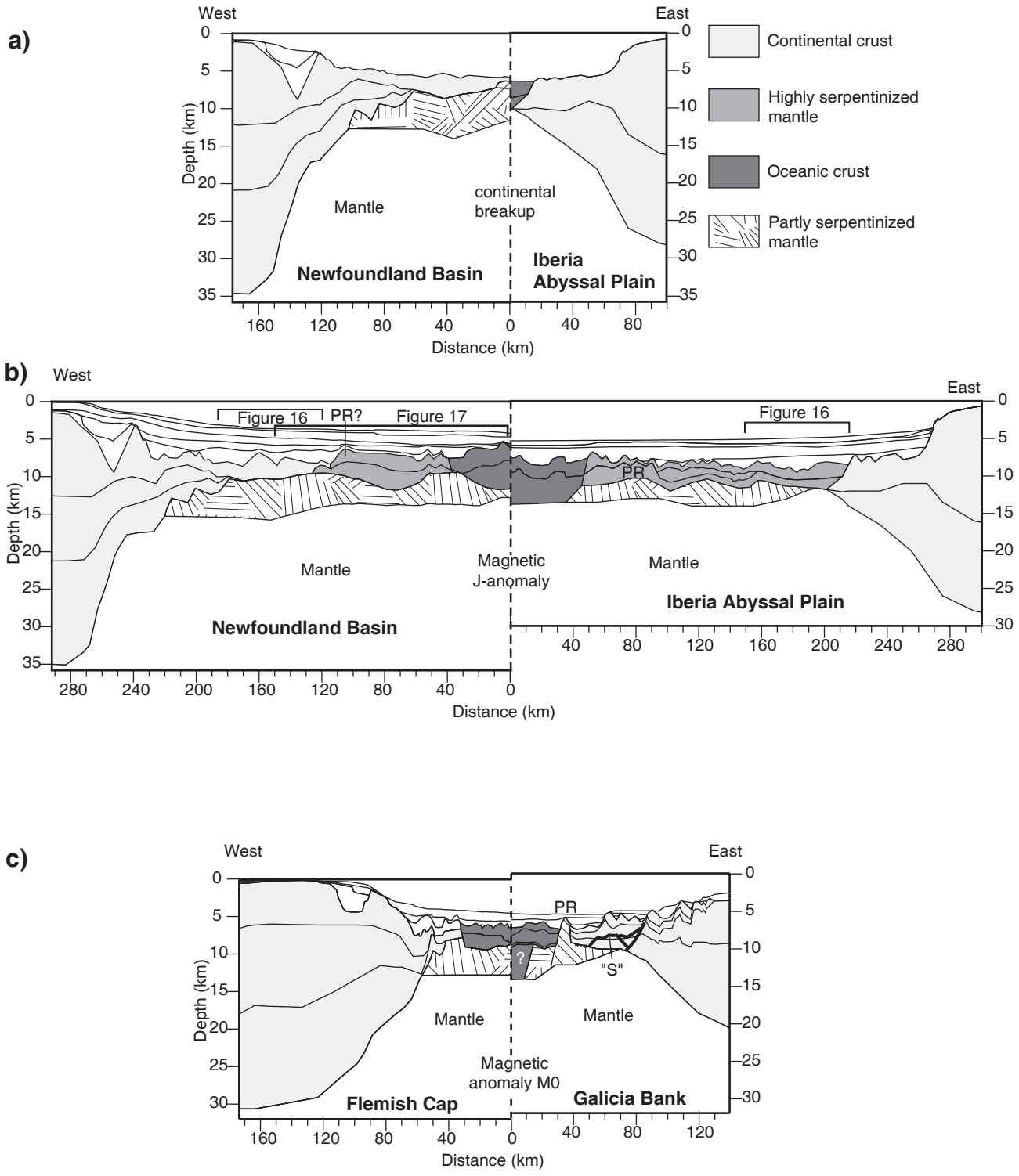
a)
West
East
Depth (km)
Continental crust
Highly serpentinized mantle
Oceanic crust
Partly serpentinized mantle
Mantle
continental breakup
Newfoundland Basin
Iberia Abyssal Plain
Distance (km)
b)
West
East
Figure 16
PR?
Figure 17
Figure 16
PR
Mantle
Magnetic J-anomaly
Mantle
Newfoundland Basin
Iberia Abyssal Plain
Depth (km)
Distance (km)
c)
West
East
PR
?
"S"
Mantle
Mantle
Magnetic anomaly M0
Flemish Cap
Galicia Bank
Depth (km)
Distance (km)

Figure 19

Appendix A – Supplementary record sections

In this appendix, record sections similar to those of Figs 3-9 are shown for OBS that are not included with the main text. This allows further assessment on constraints of the model by our data. Record sections with poor data quality (OBS 5, 8 and 18) are omitted.

Figure Caption

Figure A1. (Top) Record section for the hydrophone data of OBS 1 overlain by travel times calculated from ray tracing through the velocity model. The data have been processed with bandpass filtering (4-10 Hz). (Bottom) The corresponding ray path diagram. Note that arrivals with and without picks are both shown in solid lines. See Fig. 3 caption for other explanations of figure components.

Figure A2. (Top) Record section for the hydrophone data of OBS 2 overlain by travel times calculated from ray tracing through the velocity model. The data have been processed with bandpass filtering (4-10 Hz) and spiking deconvolution. (Bottom) The corresponding ray path diagram. See Figs 3 and A1 captions for other explanations of figure components.

Figure A3. (Top) Record section for the vertical geophone data of OBS 3 overlain by travel times calculated from ray tracing through the velocity model. The data have been processed with bandpass filtering (4-10 Hz). (Bottom) The corresponding ray path diagram. See Fig. 3 and Fig. A1 captions for other explanations of figure components.

Figure A4. (Top) Record section for the hydrophone data of OBS 26 overlain by travel times calculated from ray tracing through the velocity model. The data have been processed with bandpass filtering (4-10 Hz). (Bottom) The corresponding ray path diagram. See Fig. 3 and Fig. A1 captions for other explanations of figure components.

Figure A5. (Top) Record section for the hydrophone data of OBS 6 overlain by travel times calculated from ray tracing through the velocity model. The data have been processed with bandpass filtering (4-10 Hz) and spiking deconvolution. (Bottom) The corresponding ray path diagram. FR – floating reflector. See Fig. 3 and Fig. A1 captions for other explanations of figure components.

Figure A6. (Top) Record section for the hydrophone data of OBS 25 overlain by travel times calculated from ray tracing through the velocity model. The data have been processed with bandpass filtering (4-10 Hz). (Bottom) The corresponding ray path diagram. See Fig. 3 and Fig. A1 captions for other explanations of figure components.

Figure A7. (Top) Record section for the hydrophone data of OBS 7 overlain by travel times calculated from ray tracing through the velocity model. The data have been processed with bandpass filtering (4-10 Hz). (Bottom) The corresponding ray path diagram. See Fig. 3 and Fig. A1 captions for other explanations of figure components.

Figure A8. (Top) Record section for the vertical geophone data of OBS 9 overlain by travel times calculated from ray tracing through the velocity model. Unlike other record sections, this section is plotted with a reduction velocity of 3

km/s to show major sedimentary phases. The data have been processed with bandpass filtering (4-20 Hz). (Bottom) The corresponding ray path diagram. See Fig. 3 and Fig. A1 captions for other explanations of figure components.

Figure A9. (Top) Record section for the vertical geophone data of OBS 10 overlain by travel times calculated from ray tracing through the velocity model. The data have been processed with bandpass filtering (4-10 Hz) and spiking deconvolution. (Bottom) The corresponding ray path diagram. See Fig. 3 and Fig. A1 captions for other explanations of figure components.

Figure A10. (Top) Record section for the hydrophone data of OBS 11 overlain by travel times calculated from ray tracing through the velocity model. The data have been processed with bandpass filtering (4-10 Hz). (Bottom) The corresponding ray path diagram. See Fig. 3 and Fig. A1 captions for other explanations of figure components.

Figure A11. (Top) Record section for the hydrophone data of OBS 13 overlain by travel times calculated from ray tracing through the velocity model. The data have been processed with bandpass filtering (4-10 Hz). (Bottom) The corresponding ray path diagram. See Fig. 3 and Fig. A1 captions for other explanations of figure components.

Figure A12. (Top) Record section for the hydrophone data of OBS 14 overlain by travel times calculated from ray tracing through the velocity model. The data have been processed with bandpass filtering (4-10 Hz). (Bottom) The corresponding ray path diagram. See Fig. 3 and Fig. A1 captions for other explanations of figure components.

Figure A13. (Top) Record section for the hydrophone data of OBS 16 overlain by travel times calculated from ray tracing through the velocity model. The data have been processed with bandpass filtering (4-10 Hz) and spiking deconvolution. (Bottom) The corresponding ray path diagram. See Fig. 3 and Fig. A1 captions for other explanations of figure components.

Figure A14. (Top) Record section for the hydrophone data of OBS 22 overlain by travel times calculated from ray tracing through the velocity model. The data have been processed with bandpass filtering (4-15 Hz). (Bottom) The corresponding ray path diagram. See Fig. 3 and Fig. A1 captions for other explanations of figure components.

Figure A15. (Top) Record section for the hydrophone data of OBS 23 overlain by travel times calculated from ray tracing through the velocity model. The data have been processed with bandpass filtering (4-15 Hz). (Bottom) The corresponding ray path diagram. See Fig. 3 and Fig. A1 captions for other explanations of figure components.

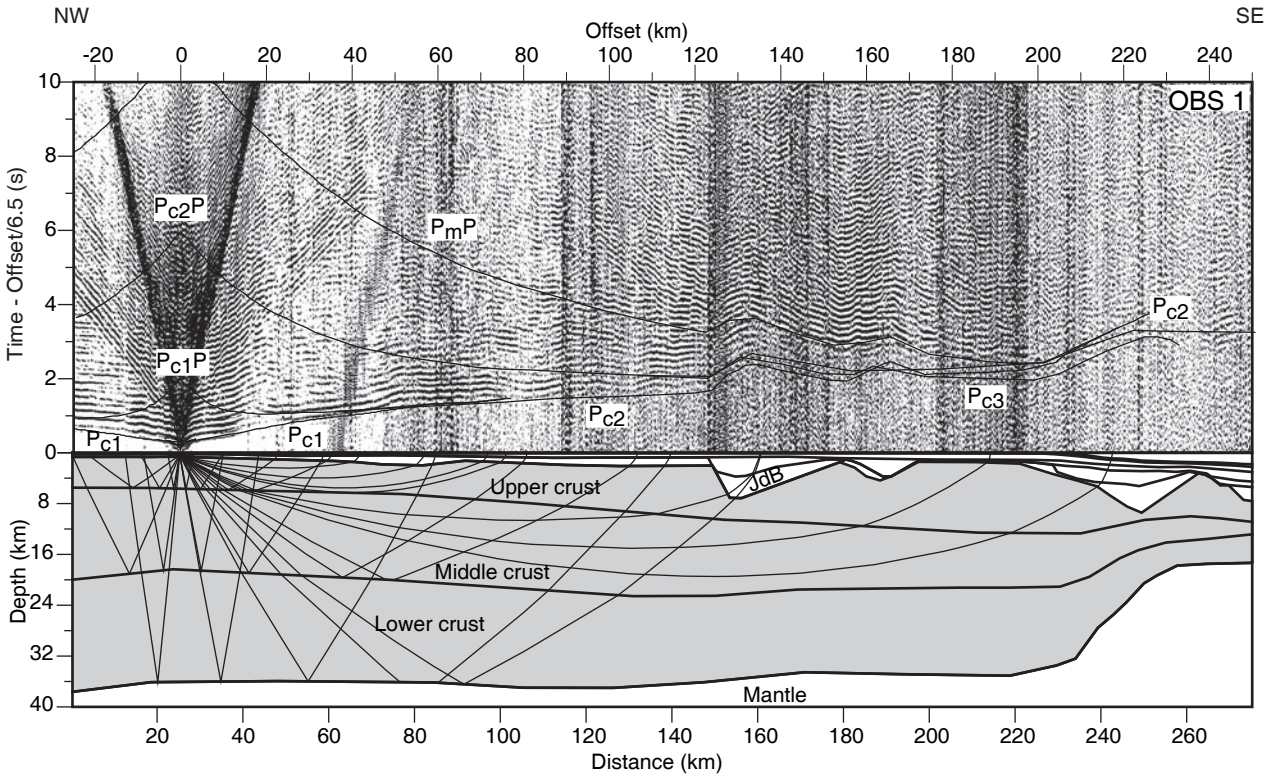
NW
SE
Offset (km)
-20
0
20
40
60
80
100
120
140
160
180
200
220
240
OBS 1
Time - Offset/6.5 (s)
10
8
6
4
2
0
$P_{c2}P$
P_mP
$P_{c1}P$
P_{c1}
P_{c1}
P_{c2}
P_{c2}
P_{c3}
Upper crust
JdB
Middle crust
Lower crust
Mantle
Depth (km)
8
16
24
32
40
20
40
60
80
100
120
140
160
180
200
220
240
260
Distance (km)

Figure A1.

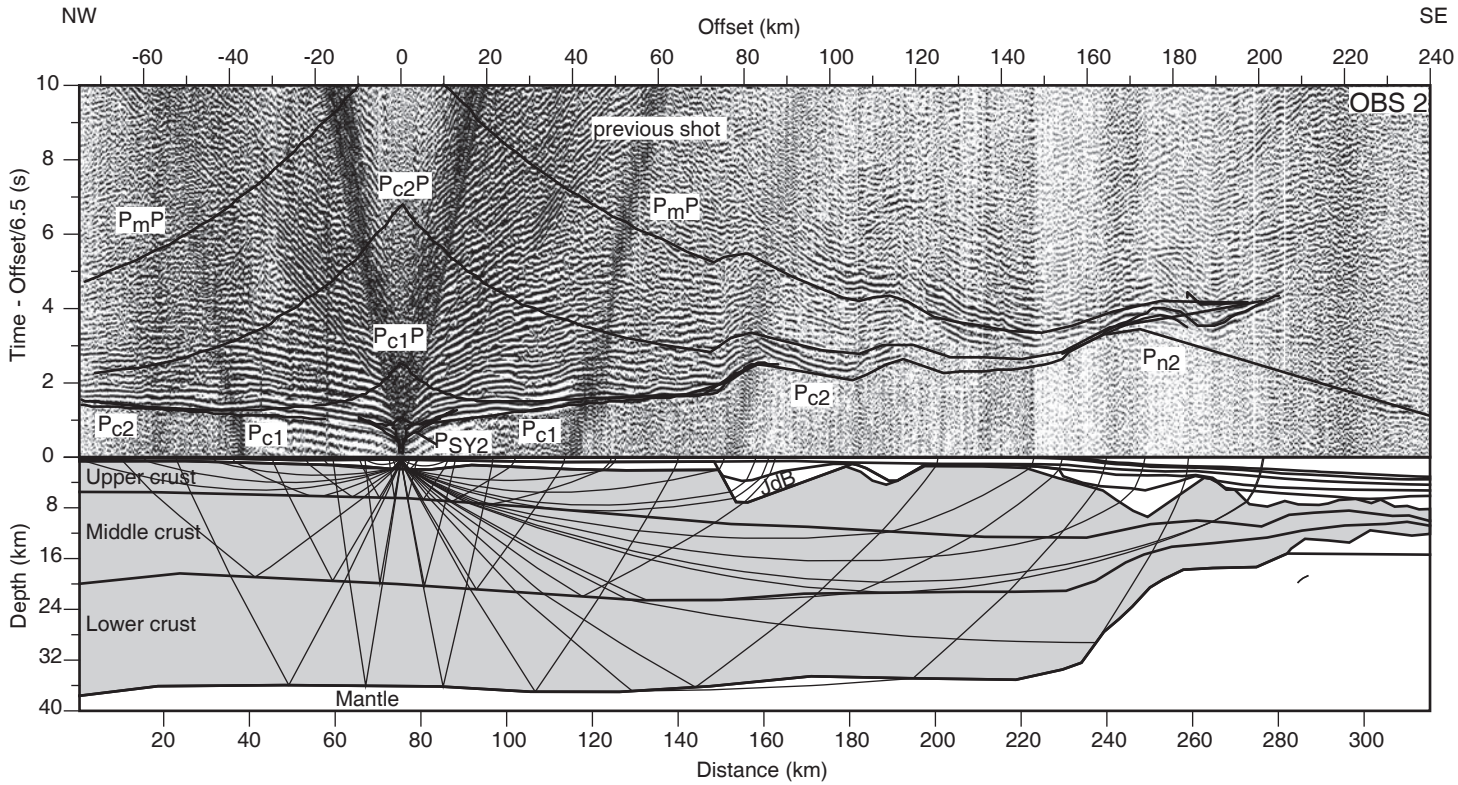
NW
SE
Offset (km)
-60 -40 -20 0 20 40 60 80 100 120 140 160 180 200 220 240
OBS 2
previous shot
$P_{c2}P$
P_mP
$P_{c1}P$
P_{n2}
P_{c2}
P_{c1}
P_{SY2}
JdB
Upper crust
Middle crust
Lower crust
Mantle
Time - Offset/6.5 (s)
Depth (km)
10 8 6 4 2 0 8 16 24 32 40
20 40 60 80 100 120 140 160 180 200 220 240 260 280 300
Distance (km)

Figure A2.

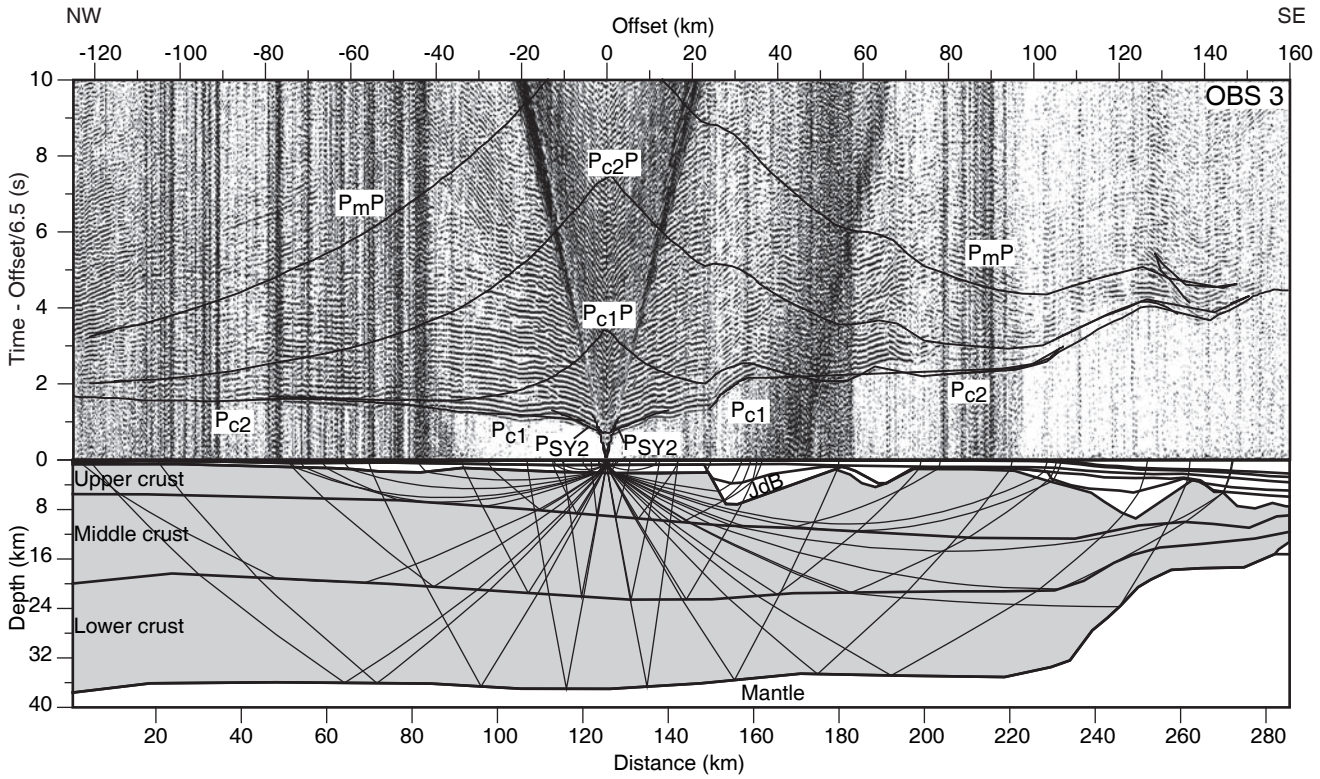
NW
SE
Offset (km)
-120 -100 -80 -60 -40 -20 0 20 40 60 80 100 120 140 160
OBS 3
Time - Offset/6.5 (s)
10 8 6 4 2 0
$P_{c2}P$
P_mP
$P_{c1}P$
P_mP
P_{c2}
P_{c1}
P_{SY2}
P_{SY2}
P_{c1}
P_{c2}
Upper crust
Middle crust
Lower crust
Mantle
JdB
Depth (km)
8 16 24 32 40
20 40 60 80 100 120 140 160 180 200 220 240 260 280
Distance (km)

Figure A3.

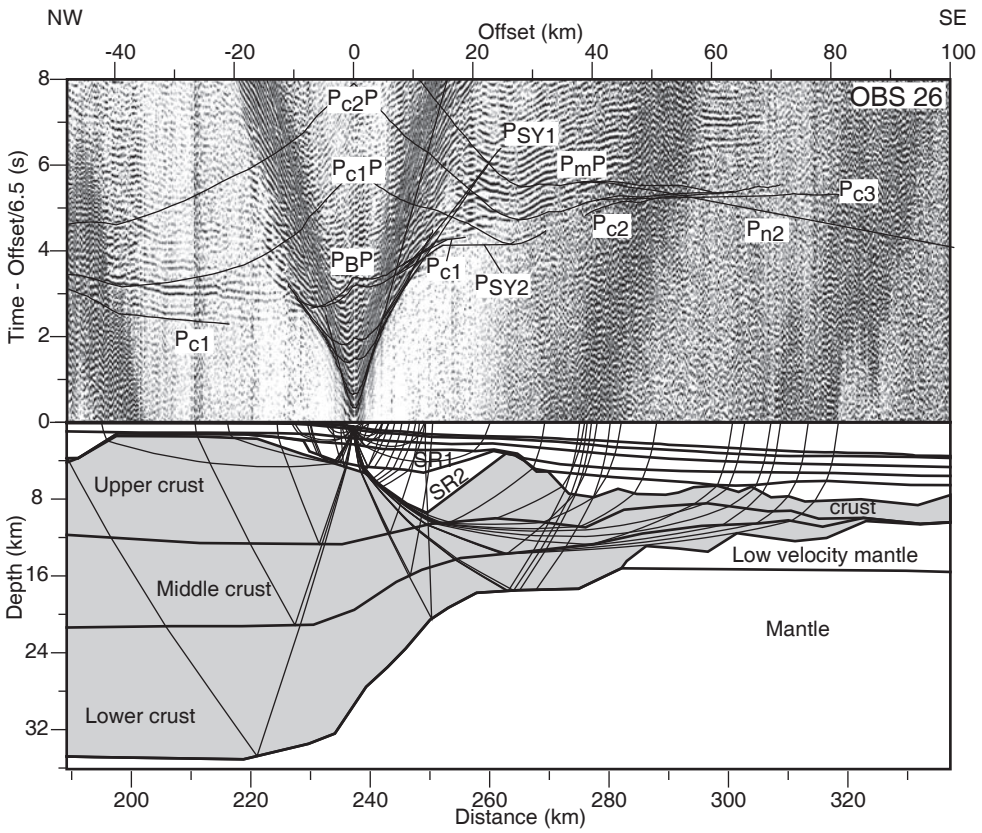
NW
SE
Offset (km)
-40
-20
0
20
40
60
80
100
OBS 26
Time - Offset/6.5 (s)
8
6
4
2
0
$P_{c2}P$
P_{SY1}
$P_{c1}P$
P_mP
P_{c3}
P_{c2}
P_{n2}
P_BP
P_{c1}
P_{SY2}
P_{c1}
SR1
SR2
Upper crust
crust
Low velocity mantle
Middle crust
Mantle
Lower crust
Depth (km)
8
16
24
32
200
220
240
260
280
300
320
Distance (km)

Figure A4.

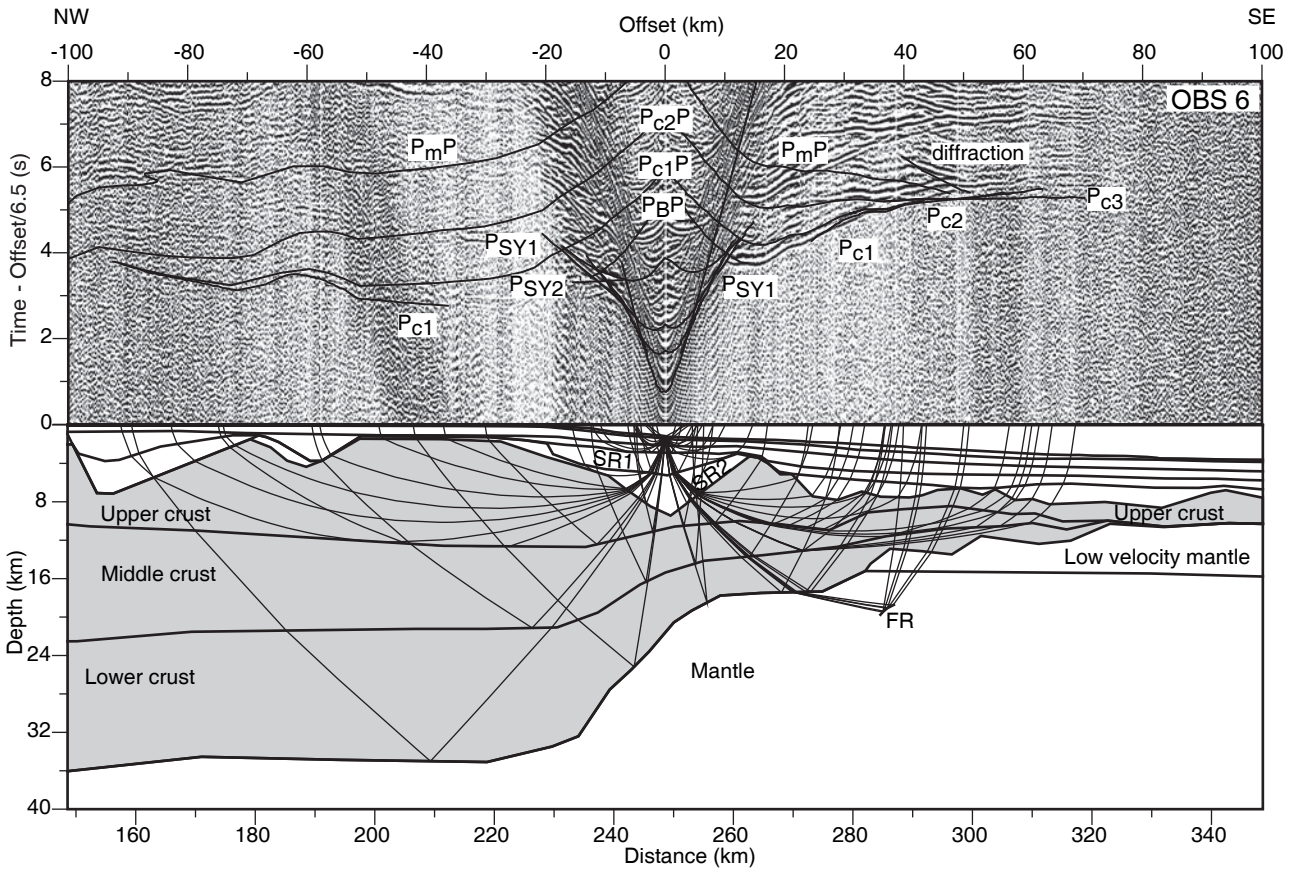
NW
SE
Offset (km)
-100
-80
-60
-40
-20
0
20
40
60
80
100
OBS 6
Time - Offset/6.5 (s)
8
6
4
2
0
P_mP
$P_{c2}P$
$P_{c1}P$
P_BP
P_{SY1}
P_{SY2}
P_{c1}
P_mP
diffraction
P_{c3}
P_{c2}
P_{c1}
P_{SY1}
SR1
cRP
Upper crust
Middle crust
Lower crust
Mantle
Upper crust
Low velocity mantle
FR
Depth (km)
8
16
24
32
40
160
180
200
220
240
260
280
300
320
340
Distance (km)

Figure A5.

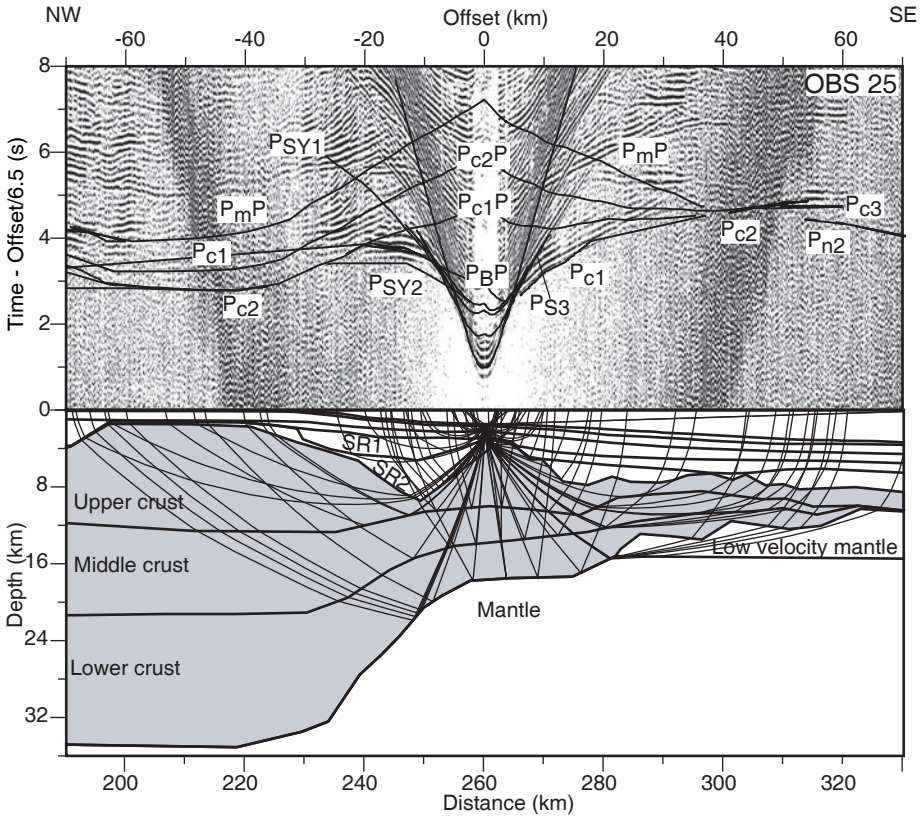
NW
SE
Offset (km)
-60
-40
-20
0
20
40
60
OBS 25
Time - Offset/6.5 (s)
8
6
4
2
0
P_{SY1}
$P_{c2}P$
P_mP
$P_{c1}P$
P_{c3}
P_mP
P_{c2}
P_{n2}
P_{c1}
P_{BP}
P_{c1}
P_{SY2}
P_{S3}
P_{c2}
SR1
SR2
Upper crust
Middle crust
Lower crust
Mantle
Low velocity mantle
Depth (km)
8
16
24
32
200
220
240
260
280
300
320
Distance (km)

Figure A6

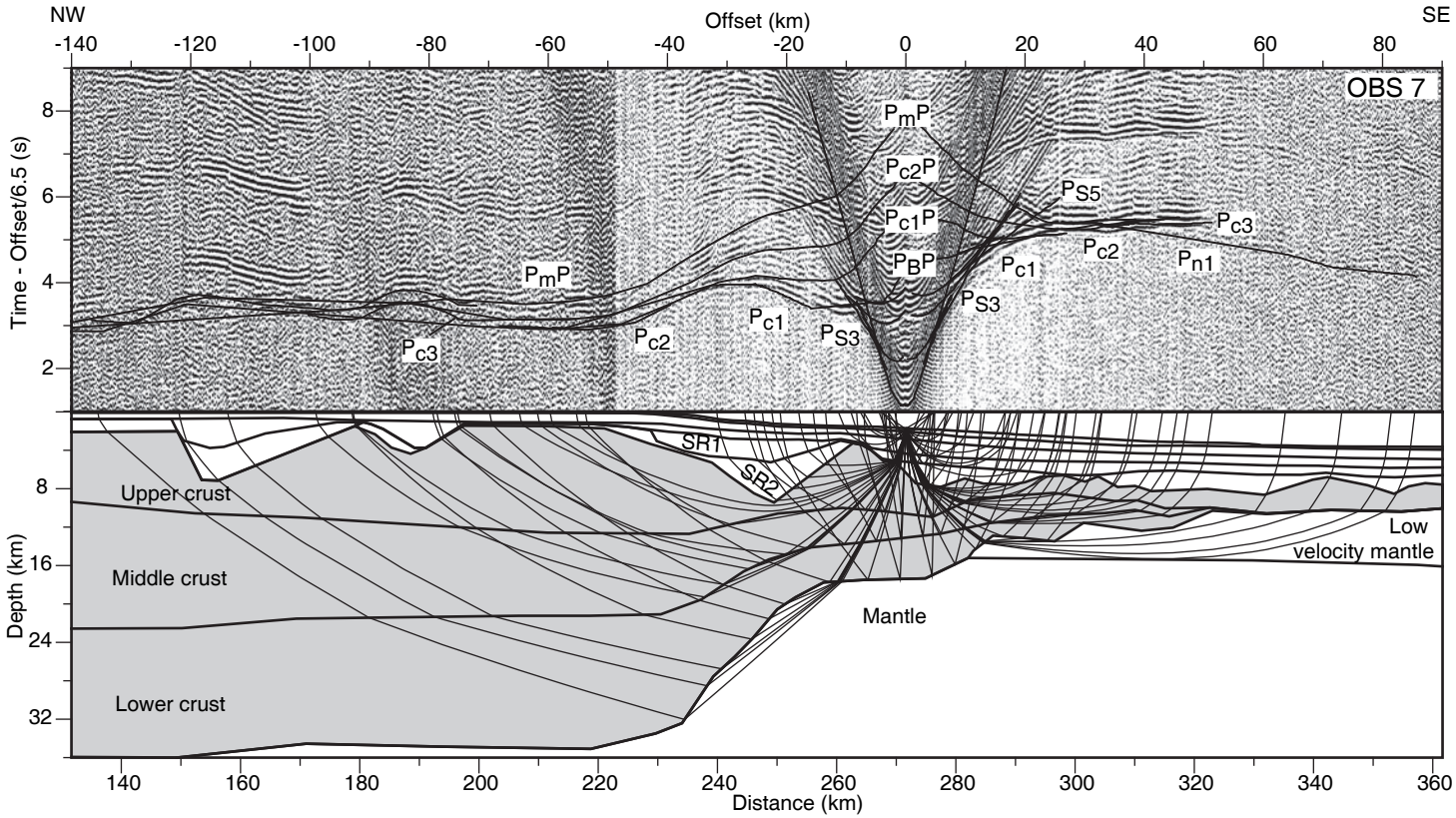
NW
SE
Offset (km)
-140
-120
-100
-80
-60
-40
-20
0
20
40
60
80
OBS 7
Time - Offset/6.5 (s)
8
6
4
2
PmP
Pc2P
Pc1P
PBP
PS5
Pc3
Pc2
Pc1
Pn1
PS3
PmP
Pc3
Pc2
Pc1
PS3
SR1
SR2
Upper crust
Middle crust
Lower crust
Mantle
Low
velocity mantle
Depth (km)
8
16
24
32
140
160
180
200
220
240
260
280
300
320
340
360
Distance (km)

Figure A7

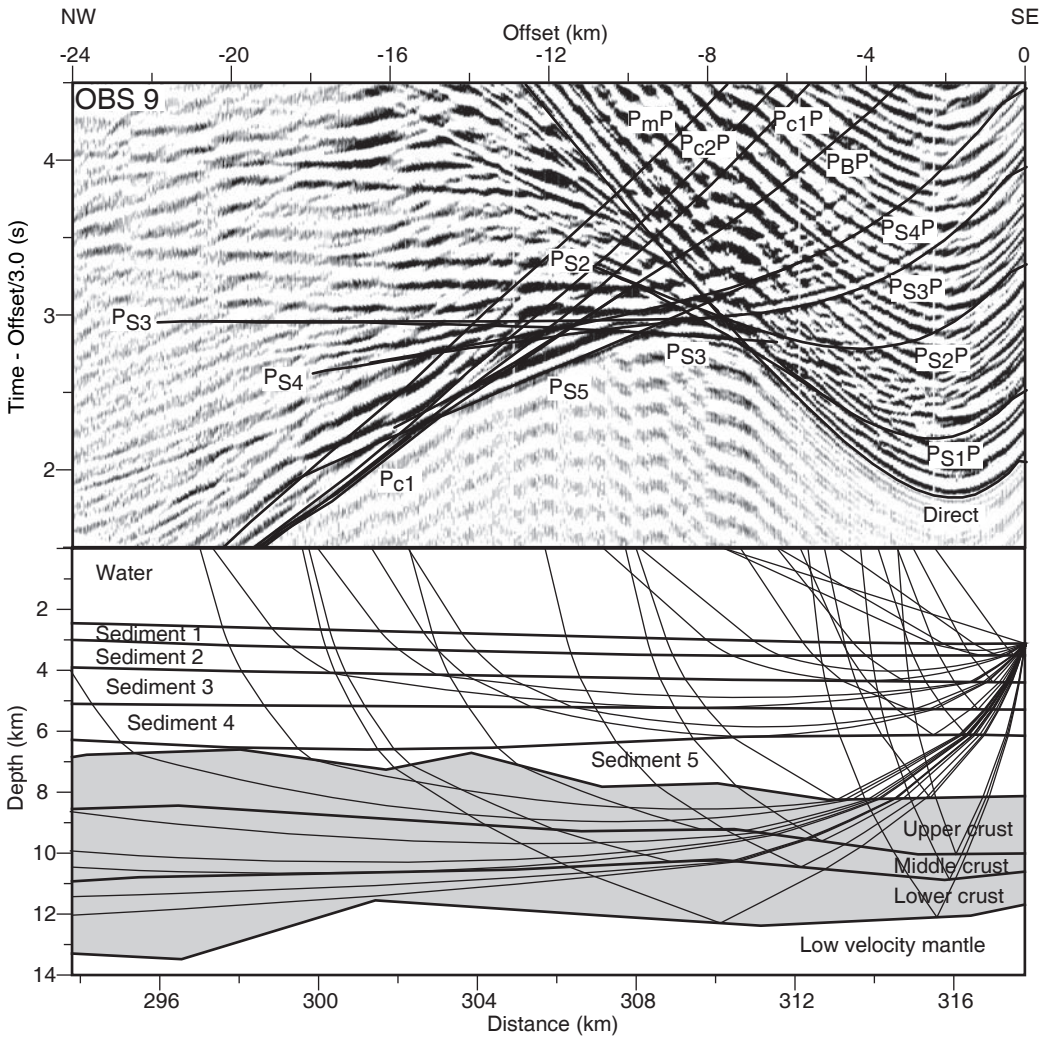
NW
SE
Offset (km)
-24
-20
-16
-12
-8
-4
0
OBS 9
PmP
Pc1P
Pc2P
PBP
PS4P
PS2
PS3P
PS3
PS3
PS2P
PS4
PS5
PS1P
Pc1
Direct
Time - Offset/3.0 (s)
4
3
2
Water
Sediment 1
Sediment 2
Sediment 3
Sediment 4
Sediment 5
Upper crust
Middle crust
Lower crust
Low velocity mantle
Depth (km)
2
4
6
8
10
12
14
296
300
304
308
312
316
Distance (km)

Figure A8

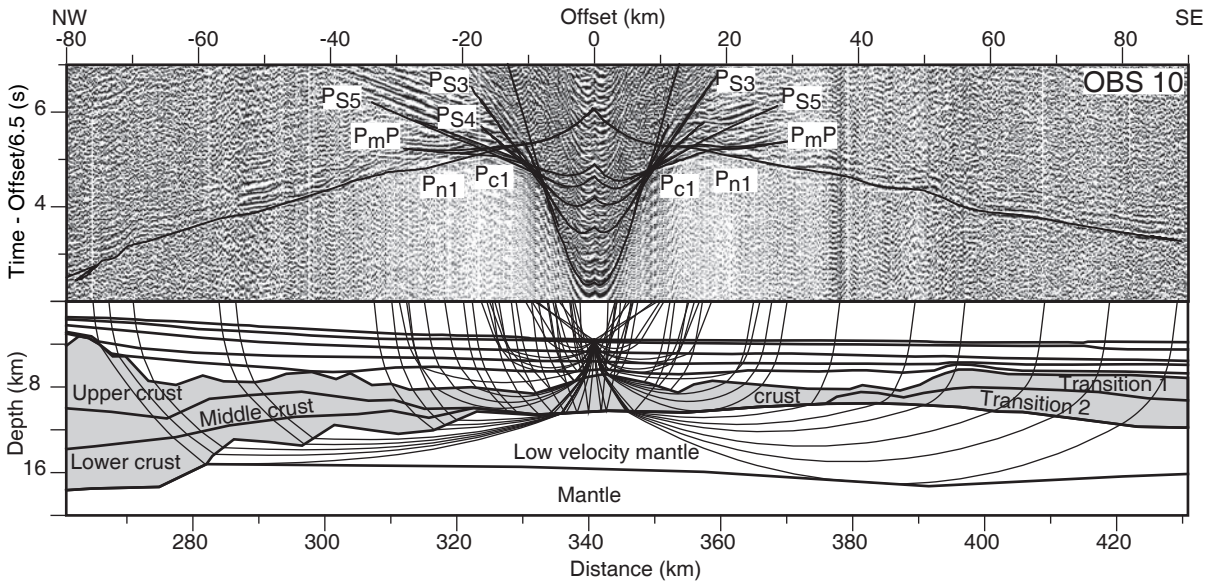
NW
SE
Offset (km)
-80
-60
-40
-20
0
20
40
60
80
OBS 10
Time - Offset/6.5 (s)
6
4
P_{S3}
P_{S5}
P_{S4}
P_mP
P_{n1}
P_{c1}
Depth (km)
8
16
Upper crust
Middle crust
Lower crust
crust
Transition 1
Transition 2
Low velocity mantle
Mantle
280
300
320
340
360
380
400
420
Distance (km)

Figure A9

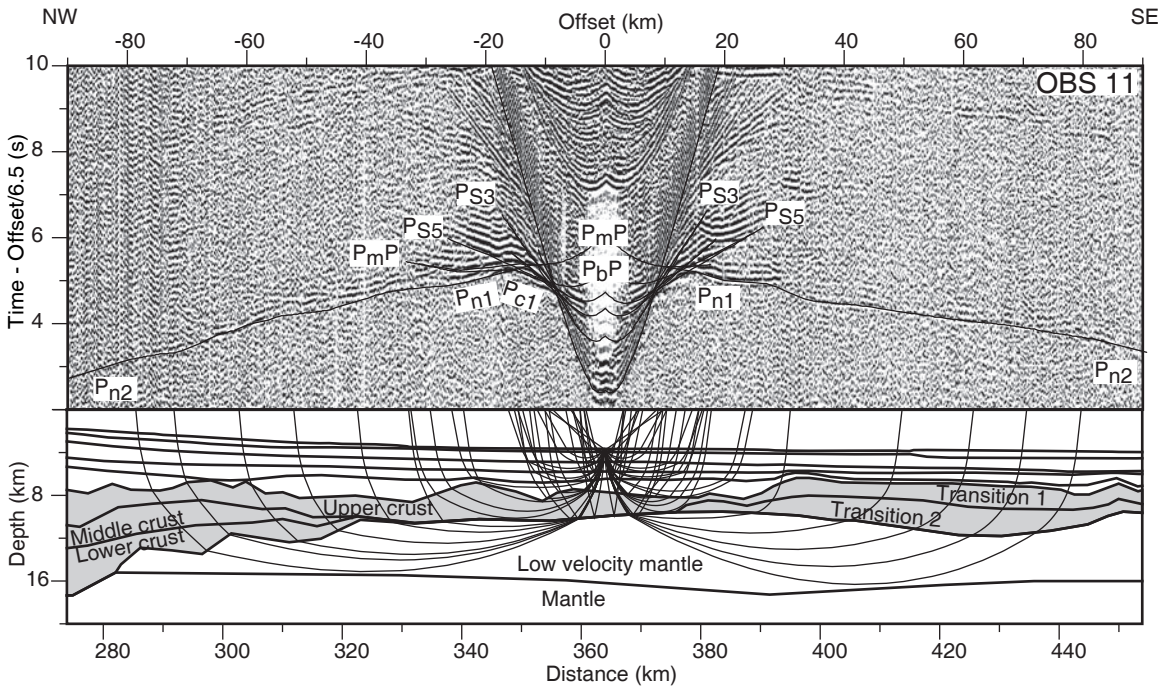
NW
SE
Offset (km)
-80
-60
-40
-20
0
20
40
60
80
OBS 11
Time - Offset/6.5 (s)
10
8
6
4
P_{S3}
P_{S5}
P_mP
P_{n1}
P_{c1}
P_bP
P_{n2}
Depth (km)
8
16
Upper crust
Middle crust
Lower crust
Transition 1
Transition 2
Low velocity mantle
Mantle
280
300
320
340
360
380
400
420
440
Distance (km)

Figure A10

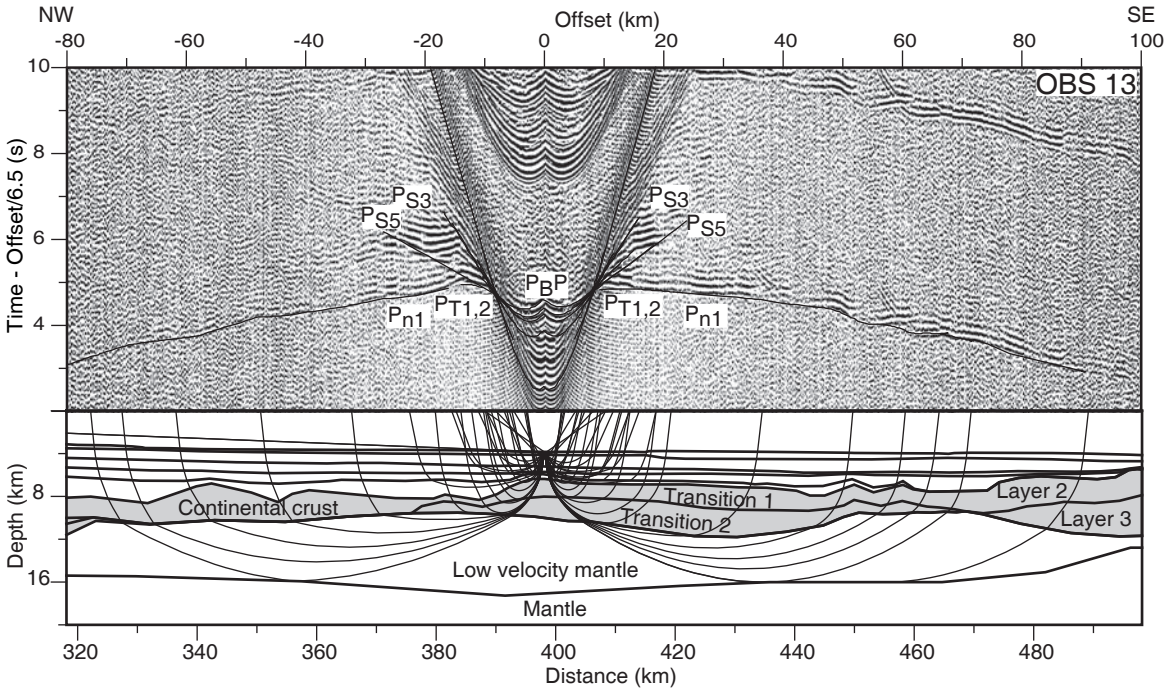
NW
SE
Offset (km)
-80
-60
-40
-20
0
20
40
60
80
100
OBS 13
Time - Offset/6.5 (s)
10
8
6
4
P_{S3}
P_{S5}
P_BP
P_{n1}
$P_{T1,2}$
Depth (km)
8
16
Continental crust
Transition 1
Transition 2
Layer 2
Layer 3
Low velocity mantle
Mantle
320
340
360
380
400
420
440
460
480
Distance (km)

Figure A11

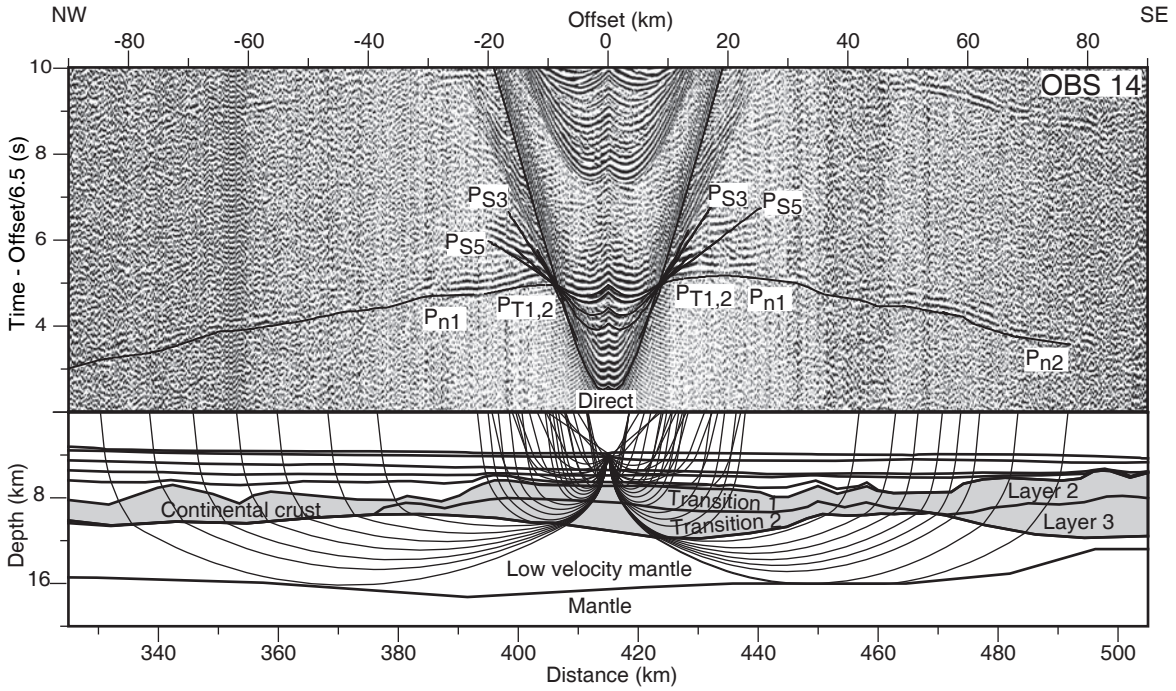
NW
SE
Offset (km)
-80
-60
-40
-20
0
20
40
60
80
OBS 14
Time - Offset/6.5 (s)
10
8
6
4
P_{S3}
P_{S5}
P_{n1}
$P_{T1,2}$
P_{n2}
Direct
Depth (km)
8
16
Continental crust
Transition 1
Transition 2
Layer 2
Layer 3
Low velocity mantle
Mantle
340
360
380
400
420
440
460
480
500
Distance (km)

Figure A12

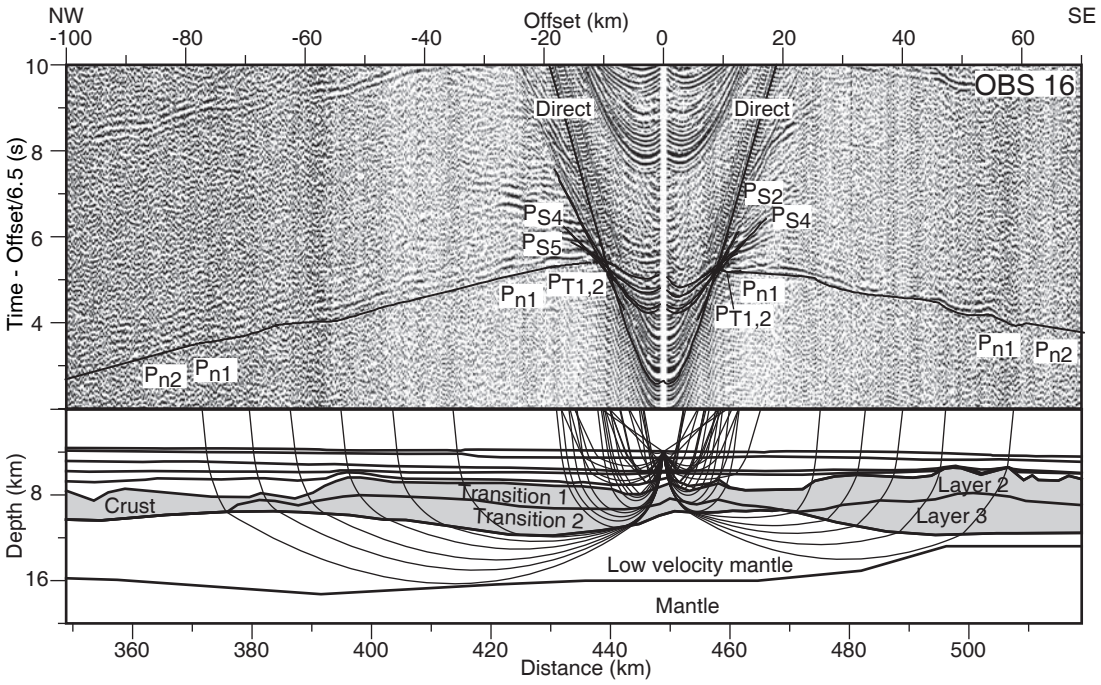
NW
SE
Offset (km)
-100
-80
-60
-40
-20
0
20
40
60
OBS 16
Direct
Direct
P_{S2}
P_{S4}
P_{S4}
P_{S5}
P_{n1}
$P_{T1,2}$
P_{n1}
$P_{T1,2}$
P_{n1}
P_{n2}
P_{n2}
P_{n1}
Time - Offset/6.5 (s)
10
8
6
4
Depth (km)
8
16
Crust
Transition 1
Transition 2
Layer 2
Layer 3
Low velocity mantle
Mantle
360
380
400
420
440
460
480
500
Distance (km)

Figure A13

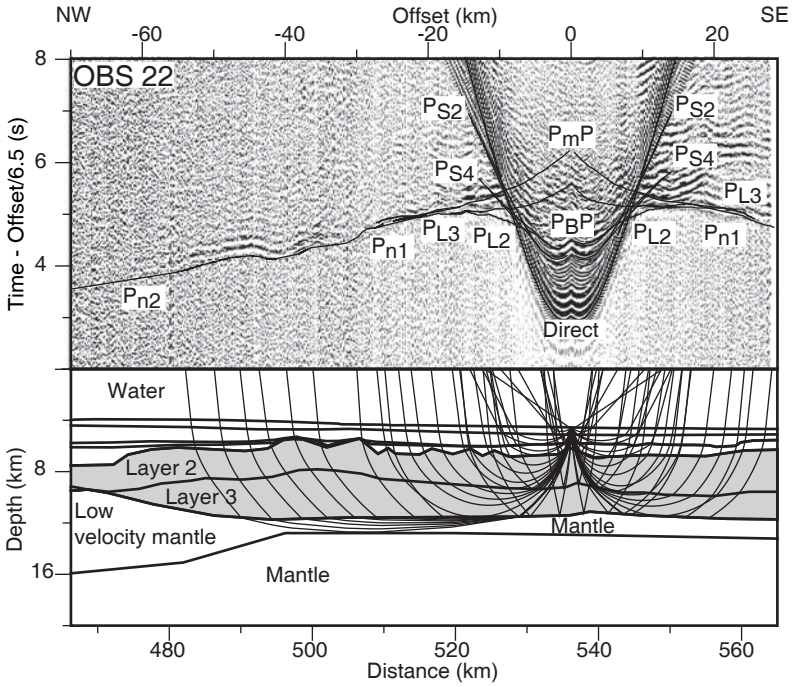
NW
Offset (km)
SE
-60
-40
-20
0
20
OBS 22
Time - Offset/6.5 (s)
8
6
4
P_{S2}
P_mP
P_{S4}
P_{L3}
P_{BP}
P_{L2}
P_{n1}
P_{n2}
Direct
Water
Layer 2
Layer 3
Low
velocity mantle
Mantle
Depth (km)
8
16
480
500
520
540
560
Distance (km)

Figure A14

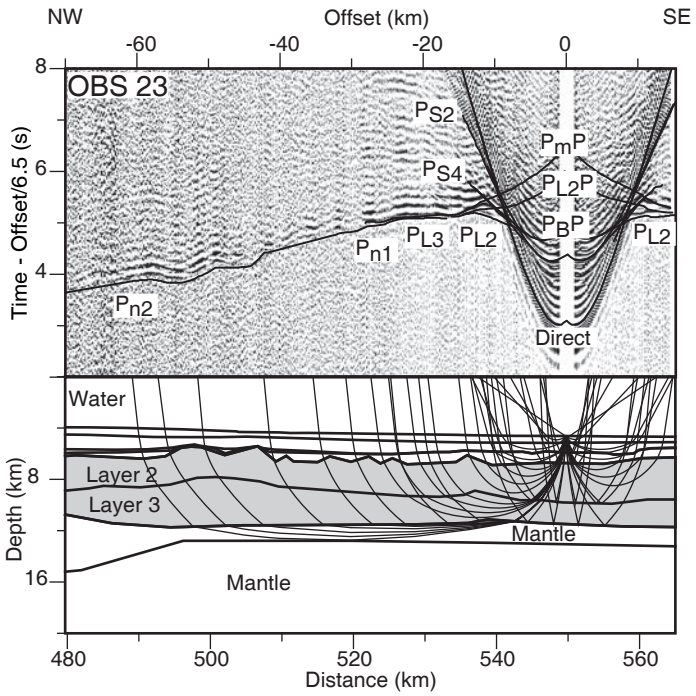
NW
Offset (km)
SE
-60
-40
-20
0
8
6
4
OBS 23
Time - Offset/6.5 (s)
P_{S2}
P_{S4}
P_{mP}
P_{L2P}
P_{BP}
P_{n1}
P_{L3}
P_{L2}
P_{L2}
P_{n2}
Direct
Water
Layer 2
Layer 3
Mantle
Mantle
Depth (km)
8
16
480
500
520
540
560
Distance (km)

Figure A15